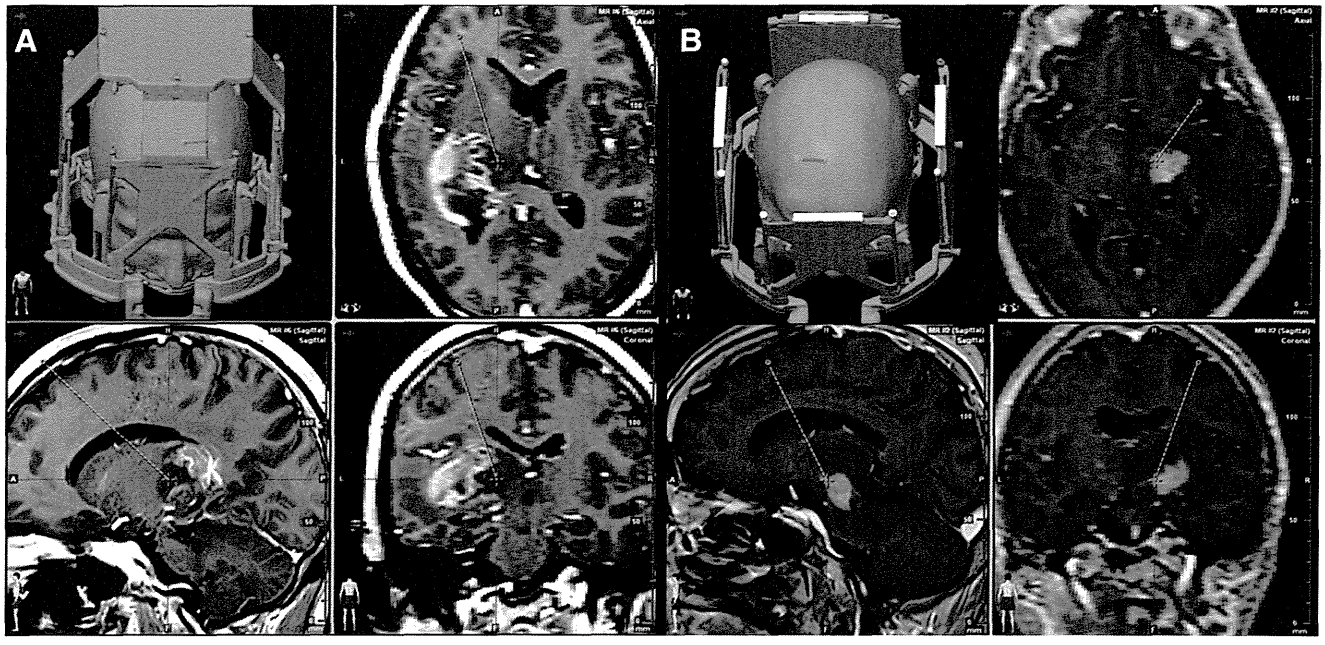

Figure 1. The iPlan Stereotaxy 2.6 software program (BrainLAB, Feldkirchen, Germany) demonstrates the tentative targets and trajectories for the stereotactic biopsy in patient 1 (**A**) and patient 2 (**B**).

trode (Radionics), a 0.5-mm diameter electrode with a 1.2-mm-diameter cannula, was fixed to the Digital Probe MicroDrive, and this electrode was stereotactically inserted along a single track. The tip of the electrode was placed into the brain 10 mm before the tentative target. The electrode was gradually inserted toward the tentative target, and the neuronal discharges were simultaneously recorded. The discharges were recorded up to just beyond the tentative target so that the circumscribed neuronal structures were sufficiently identified. The signals from the exposed tip of the electrode were sent to a NeuroMaster or NeuroPack system (Nihon-Kohden, Tokyo, Japan). The alternating neuronal discharges were detected using a bandpass filter of 20–200 Hz and a sampling rate of 1000 Hz for recording.

After recording, the NeuroMaster or NeuroPack system sent an electrical stimulation from the same electrode tip at the site of the tentative target. The electrical stimulation parameters were set at square waves of 0.2 ms duration and rates of 5 and 50 Hz. The intensity was set at 0.1 mA and was gradually increased up to 10 mA. The neurologic signs of adverse effects, such as a muscle twitch, sensory paresthesia, and gaze deviation, were monitored carefully. The actual biopsy point

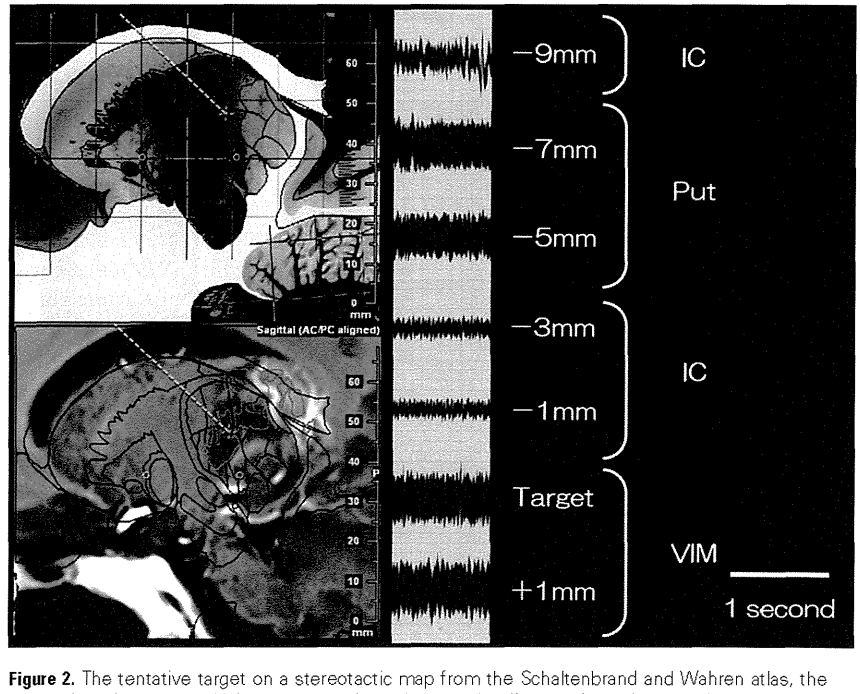

Figure 2. The tentative target on a stereotactic map from the Schaltenbrand and Wahren atlas, the alternation of neuronal discharges along the trajectory, the distance from the tentative target, and the interpretation of the neural nucleus. The tentative target is set in the dorsal thalamic VIM on a stereotactic map. The neuronal discharges change along the trajectory at the point from –9 mm to +1 mm. The trajectory is expected to pass through the IC and VIM, but the amplitude is increased at the point from –7 mm to –5 mm, thus suggesting that the electrode penetrated the putamen (Put).

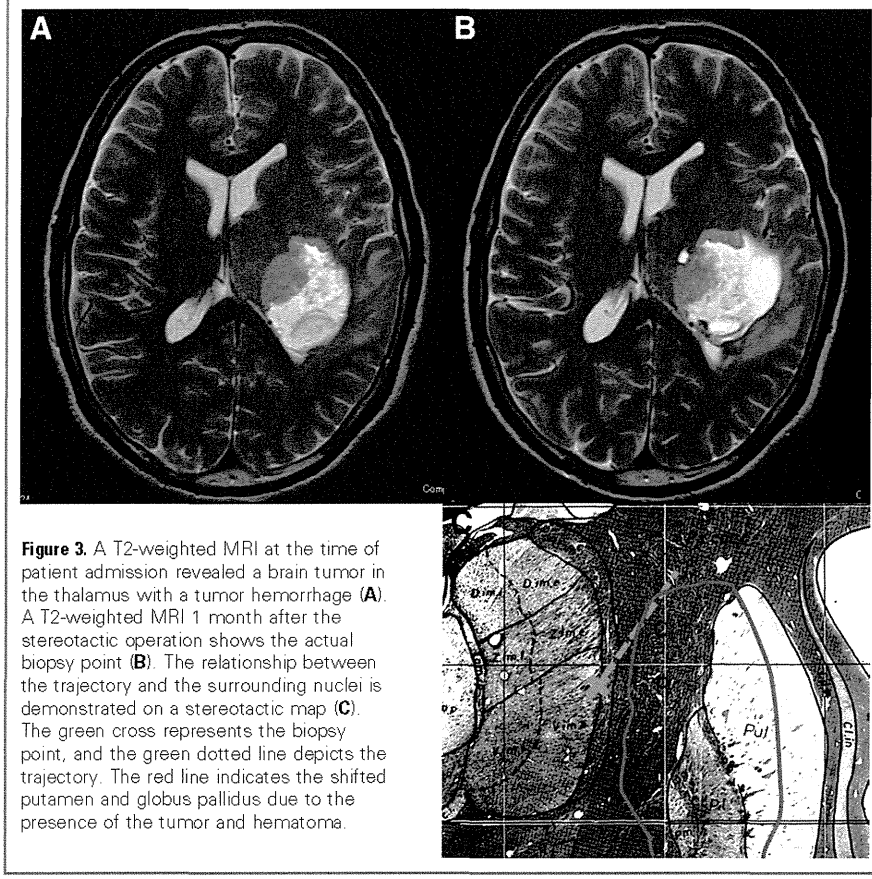

Figure 3. A T2-weighted MRI at the time of patient admission revealed a brain tumor in the thalamus with a tumor hemorrhage (**A**). A T2-weighted MRI 1 month after the stereotactic operation shows the actual biopsy point (**B**). The relationship between the trajectory and the surrounding nuclei is demonstrated on a stereotactic map (**C**). The green cross represents the biopsy point, and the green dotted line depicts the trajectory. The red line indicates the shifted putamen and globus pallidus due to the presence of the tumor and hematoma.

was assigned when no adverse event was observed. The electrode and cannula were removed after deciding the biopsy point. The Nashold Biopsy Needle (Radionics, Massachusetts, USA), a 1.8-mm-diameter cannula with a 9-mm side-slotted aperture, was stereotactically inserted along the same single track. The biopsy was routinely performed at the assigned biopsy point.

ILLUSTRATIVE CASES

Patient 1

A 34-year-old male patient presented with a progressive headache that lasted for several weeks. A neurologic examination showed a mild right homonymous hemianopsia. However, the patient's motor and sensory abilities were undisturbed. An MRI analysis revealed a diffuse astrocytoma containing an intratumoral hematoma in the left putamen and thalamus. The patient elected to undergo a tumor biopsy, because he wanted to avoid a surgical disability, such as an aggravation of the hemianopsia or a sensory or motor disturbance.

The tentative target was identified in the lesion of the thalamus and was assumed to be located in the dorsal thalamic ventralis intermedius (VIM) nucleus in front of the ventralis caudalis nucleus, on a stereotactic map from the Schaltenbrand and Wahren atlas (**Figure 2**). The trajectory was planned so that the electrode would pass through the internal capsule (IC) and the VIM. Using electrical monitoring, the amplitude of the neuronal discharges were low at a location −9 mm from the tentative target, which indicated that the electrode tip had passed through the IC. However, the amplitude level unexpectedly increased through the point from −7 to −5 mm. The amplitude returned to a low level from −3 to −1 mm, and the amplitude once more increased at the site of the tentative target (**Figure 2**). The unexpected alternation of neuronal discharges, from −7 to −5 mm, thus suggested that the electrode had penetrated the putamen, which had shifted because of the brain tumor. The low amplitude from −3 to −1 mm suggested the electrode was in the IC, and that the tentative target was located in the VIM. Electrical stimulation was administered to the tentative target, and no adverse effect was observed at low intensity. The intensity increased gradually, and sensory paresthesia was observed in part of the right proximal femoral and right lower abdomen at 6 mA. The paresthesia was aggravated and spread with 7 mA stimulation, but no other adverse effects were observed. A tentative target was thought to be separate from the ventralis caudalis and was finally determined to be a safe biopsy location. The diagnosis was anaplastic astrocytoma. The postoperative period was uneventful, and the patient received radiation therapy and chemotherapy for the remnant tumor tissue. One month later, the biopsy point was confirmed on a T2-weighted MRI (**Figure 3**).

Patient 2

An 81-year-old female patient presented with acute progressive left hemiparesis. A neurologic examination showed mild left hemiparesis and hemihypesthesia. An MRI analysis showed a Gd-enhanced lesion in the right midbrain, which was accompanied by brain edema in the surrounding structures.

The tentative target was identified as a lesion in the subthalamic nucleus (STN) (**Figure 4**). The planned trajectory was that the electrode would pass through the IC, STN, zona incerta (ZI), and substantia nigra, pars reticulata (SNr). The operation was performed with electrical monitoring as in patient 1. The amplitude of the neuronal discharge was moderate at the tentative target, but the amplitude level increased when the electrode tip passed through a point from +2 to +5 mm. The augmented amplitude decreased to a low level around a point at +6 mm, and the amplitude increased immediately at +7 mm (**Figure 4**). This suggested that the tumor had shifted the STN medially and posteriorly. The distance of the increased neuronal discharges was 3 mm, which meant the electrode tip had passed through the edge of the STN. The alternation of neuronal discharges from +6 mm to +7 mm, indicating the passage

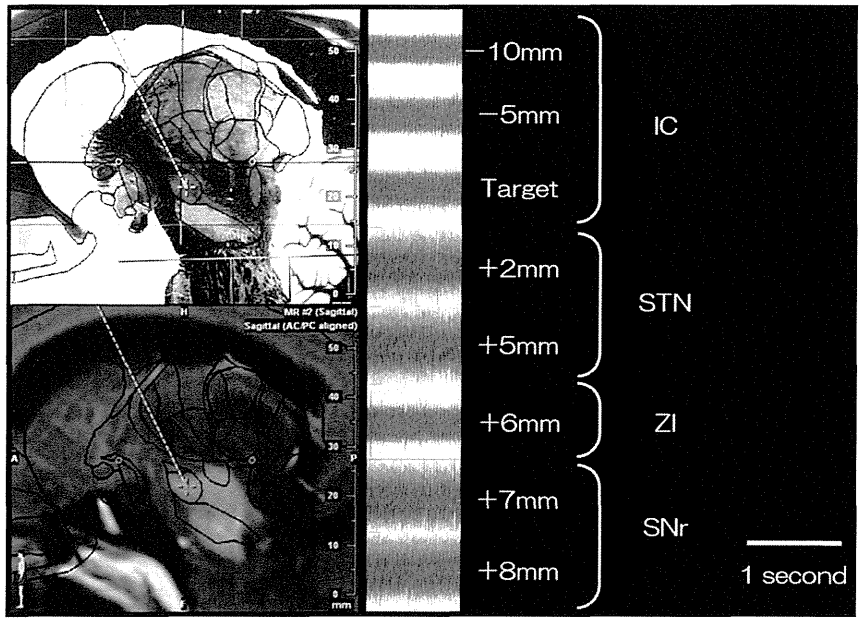

Figure 4. The tentative target is located in the center of the STN on a stereotactic map. The trajectory is expected to pass through the IC, STN, ZI, and SNr. The neuronal discharges do not increase at the point of the tentative target, thus suggesting that the STN is not located in the target. The increased discharges from +2 mm to +5 mm indicate the STN, the decreased discharges at +6 mm are in the ZI, and the increased discharges from +7 mm represent the SNr.

from the ZI to SNr (**Figure 4**). These findings suggested that the tentative target was in the IC. Electrical stimulation was administered to the tentative target. The intensity increased gradually up to 10 mA, but no adverse effects such as muscle contraction, paresthesia, or gaze deviation were observed. The tentative target was determined to be safe, and the tumor biopsy was therefore obtained. The patient's diagnosis was a malignant lymphoma. The postoperative period was uneventful, and the patient received chemotherapy for the residual tumor tissue. After tumor regression, the biopsy point was confirmed by a T2-weighted MRI (**Figure 5**).

DISCUSSION

We can accurately access deep-seated lesions using image-guided stereotactic biopsy, but we cannot identify the actual position of the trajectory and target by anatomic planning alone. Because the deep-seated lesion causes a brain shift and alters the utility of the stereotactic map, there is always a potential surgical risk that the trajectory and target may be located in the eloquent nuclei. For this reason, we used electrical recording and stimulation.

Electrical recording was established for functional neurosurgery, deep brain stimulation, and deep brain stimulation required accurate location information such as the STN, globus pallidus, and thalamus (3, 5, 8, 12, 13, 15, 17, 19). The alternations of the neuronal discharges can clearly confirm the actual trajectory and target. In the present cases, the shifted deep-seated nuclei were indicated by the unexpected alternations of the neuronal discharges along the actual trajectory and target. Patient 1 displayed a putamen that was medially shifted by the brain tumor. Patient 2 also exhibited an STN that was shifted to the posterior-medial portion. We therefore concluded that electrical recording is useful to reconcile the discrepancy between the planned and actual trajectory and target lesion in patients with deep-seated brain tumors.

In addition, electrical stimulation will also be more informative. A previous report showed that electrical stimulation could confirm whether the planned biopsy target is safe (7). The efficacy of the electrical stimulation was also confirmed in the present cases. No sensory paresthesia was observed at low current in patient 1, but was induced by stimulation with 6 mA or more. We judged that the tentative target has adequate separation from the sensory portion of the thalamus and the pyramidal tract. In patient 2, no adverse effect was observed at the tentative target after 10-mA stimulation and, therefore, this site was considered to be a safe biopsy point. Electrical stimulation may be a valuable technique in stereotactic biopsy of deep-seated lesions, although the critical level of electrical stimulation has not been established.

A stereotactic biopsy can be performed safely without any complications. Therefore, it is important to recognize the accurate positions of the trajectory and target during a biopsy of deep-seated lesions. The electrical monitoring will enable accurate positioning and will help minimize the risk of injury to the adjacent significant nuclei. The number of trajectories may be also minimized if the first trajectory and target are not appropriate, because the actual trajectory could be more reliable and yield additional information based on the electrical findings of the previous trajectory. Electrical monitoring will be a highly useful technique in conjunction with ordinary image-guided biopsies. Conversely, this method may increase the risk of hematoma following the penetration of the electrical needle into tumor, although we believe this risk is minimal.

The electrical monitoring is a useful and safe method, considering the following conditions:

1. The deep-seated lesion causes the brain to shift and alters the utility of the stereotactic map.
2. The planned trajectory and target are located in or close to the eloquent nuclei.
3. The patient is conscious and can tolerate to be awake during the surgery.

CONCLUSION

The current report described two patients with deep-seated brain tumors who underwent a stereotactic biopsy. The patients were monitored with electrical recording

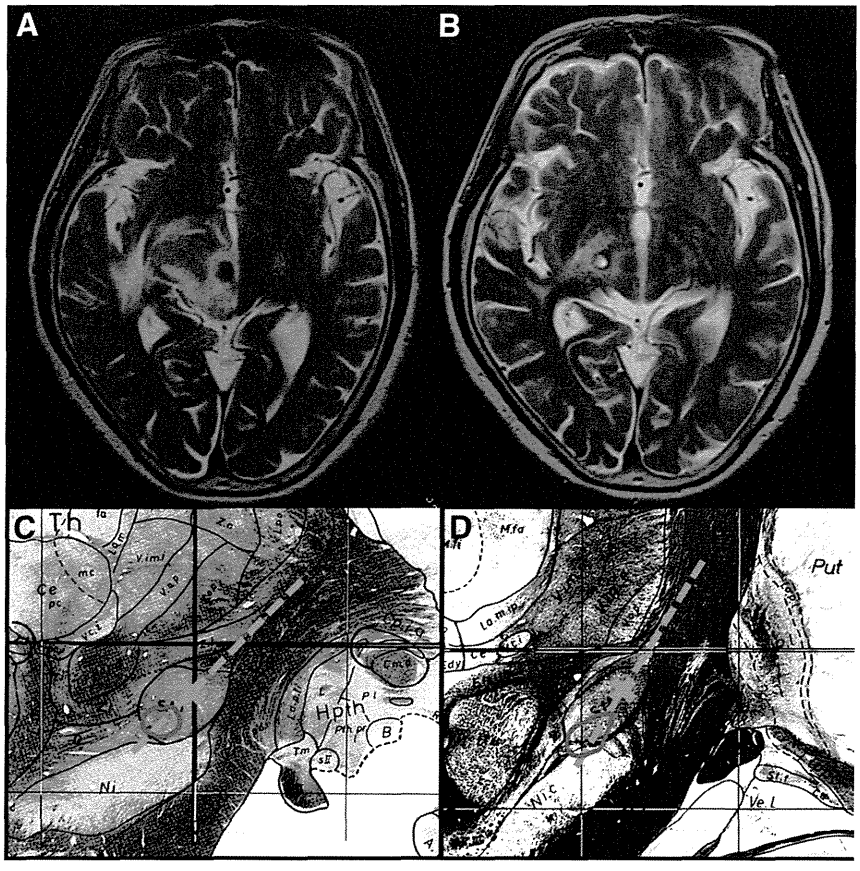

Figure 5. A T2-weighted MRI at the time of patient admission shows a brain tumor in the right midbrain (**A**), and an MRI 1 month after the stereotactic operation shows the actual biopsy point (**B**). The relationship between the trajectory and surrounding nuclei is demonstrated in the sagittal (**C**) and coronal (**D**) sections. The green cross indicates the biopsy point, and the green dotted line is the trajectory. The red line indicates the shifted STN.

and stimulation, and the biopsies were successfully performed without inducing any neurologic deficits.

REFERENCES

1. Apuzzo ML, Chandrasoma PT, Cohen D, Zee CS, Zelman V: Computed imaging stereotaxy: experience and perspective related to 500 procedures applied to brain masses. Neurosurgery 20:930-7, 1987.

2. Apuzzo ML, Sabshin JK: Computed tomographic guidance stereotaxis in the management of intracranial mass lesions. Neurosurgery 12:277-85, 1983.

3. Benazzouz A, Breit S, Koudsie A, Pollak P, Krack P, Benabid AL: Intraoperative microrecordings of the subthalamic nucleus in Parkinson's disease. Mov Disord 17(Suppl 3):S145-9, 2002.

4. Coffey RJ, Lunsford LD: Stereotactic surgery for mass lesions of the midbrain and pons. Neurosurgery 17:12-8, 1985.

5. Gross RE, Krack P, Rodriguez-Oroz MC, Rezai AR, Benabid AL: Electrophysiological mapping for the implantation of deep brain stimulators for Parkinson's disease and tremor. Mov Disord 21(Suppl 14): S259-83, 2006.

6. Hall WA: The safety and efficacy of stereotactic biopsy for intracranial lesions. Cancer 82:1749-55, 1998.

7. Hood TW, Gebarski SS, Mckeever PE, Venes JL: Stereotaxic biopsy of intrinsic lesions of the brain stem. J Neurosurg 65:172-6, 1986.

8. Hutchison WD, Allan RJ, Opitz H, Levy R, Dostrovsky JO, Lang AE, Lozano AM: Neurophysiological identification of the subthalamic nucleus in surgery for Parkinson's disease. Ann Neurol 44: 622-8, 1998.

9. Kelly PJ: Stereotactic biopsy and resection of thalamic astrocytomas. Neurosurgery 25:185-95, 1989.

10. Kim JE, Kim DG, Paek SH, Jung HW: Stereotactic biopsy for intracranial lesions: reliability and its impact on the planning of treatment. Acta Neurochir 145:547-54, 2003.

11. Kondziolka D, Lunsford LD: Results and expectations with image-integrated brainstem stereotactic biopsy. Surg Neurol 43:558-62, 1995.

12. Lenz FA, Jaeger CJ, Seike MS, Lin YC, Reich SG: Single-neuron analysis of human thalamus in patients with intention tremor and other clinical signs of cerebellar disease. J Neurophysiol 87:2084-94, 2002.

13. Lozano A, Hutchison W, Kiss Z, Tasker R, Davis K, Dostrovsky J: Methods for microelectrode-guided posteroventral pallidotomy. J Neurosurg 84:194-202, 1996.

14. McGirt MJ, Woodworth GF, Coon AL, Frazier JM, Amundson E, Garonzik I, Olivi A, Weingart JD: Independent predictors of morbidity after image-guided stereotactic brain biopsy: a risk assessment of 270 cases. J Neurosurg 102:897-901, 2005.

15. Pollak P, Krack P, Fraix V, Mendes A, Moro E, Chabardes S, Benabid AL: Intraoperative micro- and macrostimulation of the subthalamic nucleus in Parkinson's disease. Mov Disord 17(Suppl 3):S155-61, 2002.

16. Sawin PD, Hitchon PW, Follett KA, Torner JC: Computed imaging-assisted stereotactic brain biopsy: a risk analysis of 225 consecutive cases. Surg Neurol 49:640-9, 1998.

17. Starr PA, Turner RS, Rau G, Lindsey N, Heath S, Volz M, Ostrem JL, Marks WJ Jr: Microelectrode-guided implantation of deep brain stimulators into the globus pallidus internus for dystonia: techniques, electrode locations, and outcomes. J Neurosurg 104: 488-501, 2006.

18. Steck J, Friedman WA: Stereotactic biopsy of brainstem mass lesions. Surg Neurol 43:563-7, 1995.

19. Vitek JL, Bakay RA, Hashimoto T, Kaneoke Y, Mewes K, Zhang JY, Rye D, Starr P, Baron M, Turner R, DeLong MR: Microelectrode-guided pallidotomy: technical approach and its application in medically intractable Parkinson's disease. J Neurosurg 88: 1027-43, 1998.

Conflict of interest statement: The authors declare that the article content was composed in the absence of any commercial or financial relationships that could be construed as a potential conflict of interest.

Received 15 January 2010; accepted 03 May 2010

Citation: World Neurosurg. (2013) 79, 1:207.e1-207.e5.

DOI: 10.1016/j.wneu.2010.05.028

Journal homepage: ***www.WORLDNEUROSURGERY.org***

Available online: ***www.sciencedirect.com***

1878-8750/$ - see front matter *© 2013 Elsevier Inc. All rights reserved.*

In vivo fluorescence resonance energy transfer imaging reveals differential activation of Rho-family GTPases in glioblastoma cell invasion

Eishu Hirata[1], Hiroko Yukinaga[2], Yuji Kamioka[1], Yoshiki Arakawa[3], Susumu Miyamoto[3], Takaharu Okada[4], Erik Sahai[5] and Michiyuki Matsuda[1,2,*]

[1]Department of Bioimaging and Cell Signaling, Graduate School of Biostudies, Kyoto University, Kyoto, 606-8501, Japan
[2]Department of Pathology and Biology of Diseases, Graduate School of Medicine, Kyoto University, Kyoto, 606-8501, Japan
[3]Department of Neurosurgery, Graduate School of Medicine, Kyoto University, Kyoto, 606-8507, Japan
[4]Research Unit for Immunodynamics, RIKEN Research Center for Allergy and Immunology, Yokohama, 230-0045, Japan
[5]Tumour Cell Biology Laboratory, Cancer Research UK London Research Institute, London, WC2A 3PX, UK
*Author for correspondence (matsudam@lif.kyoto-u.ac.jp)

Accepted 17 August 2011
Journal of Cell Science 125, 858–868
© 2012. Published by The Company of Biologists Ltd
doi: 10.1242/jcs.089995

Summary

Two-photon excitation microscopy was used to visualized two different modes of invasion at perivascular and intraparenchymal regions of rat C6 glioblastoma cells that were orthotopically implanted into rat brains. Probes based on the principle of Förster resonance energy transfer (FRET) further revealed that glioblastoma cells penetrating the brain parenchyma showed higher Rac1 and Cdc42 activities and lower RhoA activity than those advancing in the perivascular regions. This spatial regulation of Rho-family GTPase activities was recapitulated in three-dimensional spheroid invasion assays with rat and human glioblastoma cells, in which multipod glioblastoma cells that invaded the gels and led the other glioblastoma cells exhibited higher Rac1 and Cdc42 activities than the trailing glioblastoma cells. We also studied the Cdc42-specific guanine nucleotide exchange factor Zizimin1 (also known as DOCK9) as a possible contributor to this spatially controlled activation of Rho-family GTPases, because it is known to play an essential role in the extension of neurites. We found that shRNA-mediated knockdown of Zizimin1 inhibited formation of pseudopodia and concomitant invasion of glioblastoma cells both under a 3D culture condition and in vivo. Our results suggest that the difference in the activity balance of Rac1 and Cdc42 versus RhoA determines the mode of glioblastoma invasion and that Zizimin1 contributes to the invasiveness of glioblastoma cells with high Rac1 and Cdc42 activities.

Key words: Glioblastoma, Invasion, Rho-family GTPase, FRET, Zizimin1 (DOCK9)

Introduction

The most common and aggressive human primary brain tumor is the glioblastoma, which invades extremely rapidly and culminates in the death of patients usually within a year after diagnosis (Louis et al., 2007). Glioblastoma was previously called glioblastoma 'multiforme', reflecting its histopathological divergence in size, shape, karyotype, etc. Glioblastomas invade either around the vascular space or along neuronal fibers into the brain parenchyma (Bellail et al., 2004; Furnari et al., 2007). Among many experimental models of human glioblastoma, the allograft model of rat C6 glioblastoma cells is used most extensively (Grobben et al., 2002). The C6 glioblastoma cells implanted into syngeneic Wistar rats share many histological hallmarks with human glioblastoma and preferentially migrate along neuronal fibers and through the perivascular region, which resembles the spread of human glioblastoma.

Various types of cancer cell exhibit diverse invasion morphologies with great plasticity not only in the tissues but also in the three-dimensional (3D) substrate (Sahai and Marshall, 2003; Friedl and Wolf, 2010). Rho-family GTPases are considered to play the central role in the regulation of invasion (Sahai et al., 2007; Croft and Olson, 2008; Sanz-Moreno et al., 2008), probably through cytoskeletal reorganization (Sahai and Marshall, 2003; Kurokawa and Matsuda, 2005; Pertz et al., 2006; Machacek et al., 2009). It has also been documented that coordinated activation and/or antagonistic action of Rho-family GTPases determine the invasion modes of various cancer cell types in the 3D environment (Sahai et al., 2007; Croft and Olson, 2008; Sanz-Moreno et al., 2008). However, the activity of Rho-family GTPases in vivo or in 3D substrate has never been successfully shown in mammals. Consequently, the spatial regulation of Rho-family GTPase in cancer tissues is unknown.

We and others have been developing biosensors based on the principle of Förster resonance energy transfer (FRET) for Ras-superfamily GTPases (Aoki and Matsuda, 2009). These biosensors, which are collectively called Ras and interacting protein chimeric unit (Raichu), have been successfully used to visualize the spatiotemporal regulation of Rho-family GTPases within MDCK cells (Kurokawa and Matsuda, 2005), zebrafish (Miyagi et al., 2004) and *Drosophila melanogaster* (Kamiyama and Chiba, 2009). However, there was a fatal flaw in the

Journal of Cell Science

application of the current FRET biosensors to 3D imaging: stable transfectants of FRET biosensors are not readily obtained when fluorescent proteins derived from *Aequorea victoria* are used as the FRET donor and acceptor proteins (Aoki and Matsuda, 2009). To circumvent this problem, we have developed FRET biosensors with a teal fluorescent protein (TFP) as a FRET donor and succeeded in establishing C6 glioblastoma cell lines expressing FRET biosensors. With these newly developed FRET biosensors, we demonstrate that two different invasion modes of glioblastoma cells can be achieved by the activity balance of Rac1 and Cdc42 versus RhoA. This spatially biased activity is at least partly dependent on Zizimin1 (also known as DOCK9), a Cdc42-specific guanine nucleotide exchange factor.

Results

Time-lapse two-photon microscopy revealed different invasion modes in the perivascular region and parenchymal tissue

C6 glioblastoma cells expressing GFP as a marker were grafted into rat brains and after 7 days were observed ex vivo by the brain slice culture technique. The transplanted C6 glioblastoma cells looked poorly delineated macroscopically (Fig. 1A). However, under a two-photon microscope, glioblastoma cells could be seen to have advanced preferentially along blood vessels at the invasion front (Fig. 1B,C), and had often penetrated the brain parenchyma from the perivascular region (arrowheads in Fig. 1C). Time-lapse images revealed that glioblastoma cells

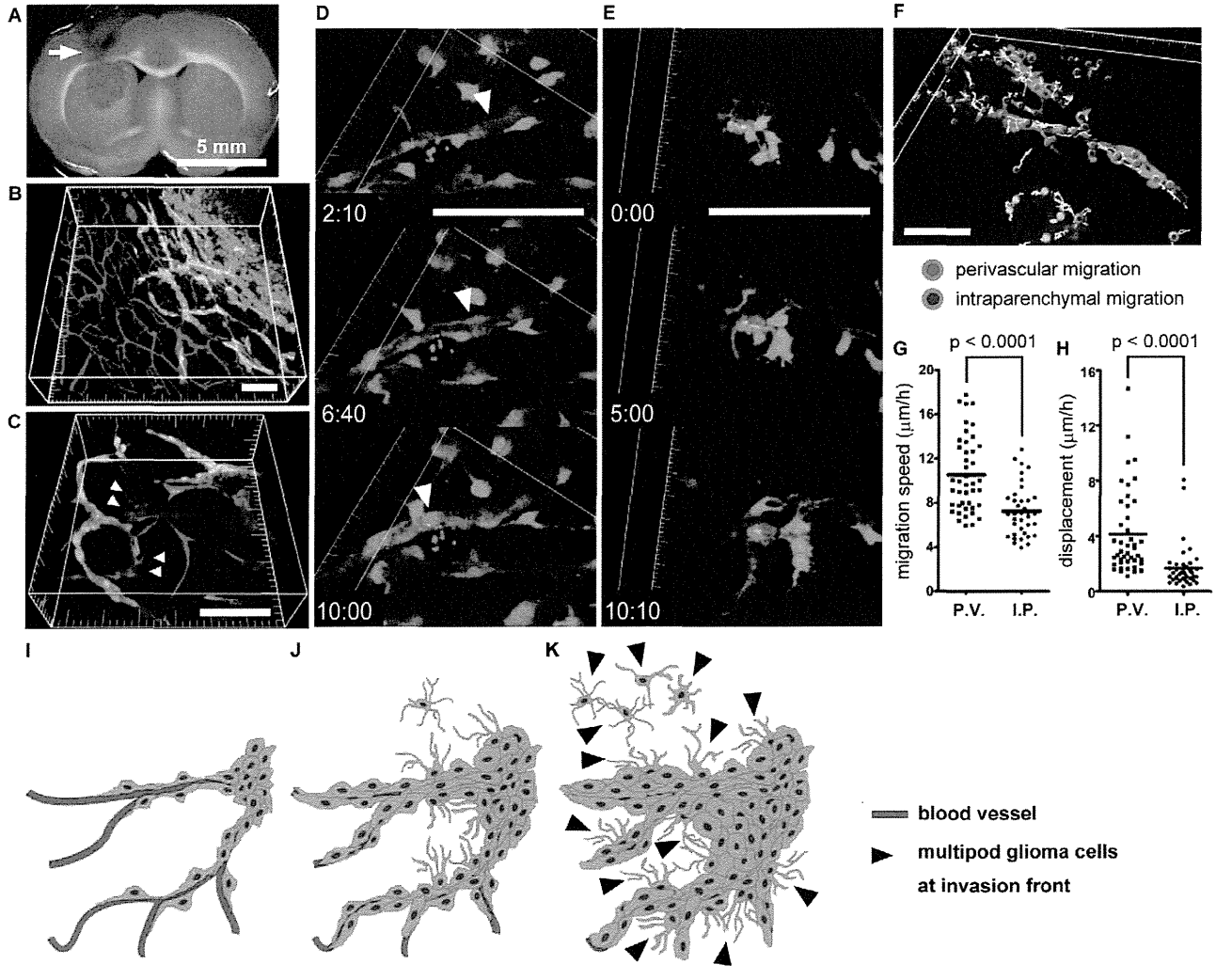

Fig. 1. Time-lapse two-photon microscopy revealed different invasion modes in the perivascular region and parenchymal tissue. (**A**) C6 glioblastoma cells stably expressing mEGFP formed an invasive tumor mass in rat brains 7 days after inoculation (arrow). (**B**,**C**) The invasion front of the tumor was imaged under a two-photon excitation microscope. An enlarged view is shown in C. C6 glioblastoma cells are shown in green and blood vessels, labeled with Texas-Red-conjugated dextran are red. (**D**,**E**) Time-lapse images revealed that the invasion morphologies of C6 glioblastoma cells in the perivascular space (D) were different from those in the parenchymal tissue (E). Blood vessels are shown in red in both figures. (**F**) Invading C6 glioblastoma cells at the periphery of the tumor mass were classified into two groups: a perivascular invasion group and intraparenchymal invasion group (colored red and blue, respectively). Time-lapse images were corrected for drift, and migration speed (μm/hour) and net displacement (μm/hour) were quantitatively analyzed, and are shown in **G** and **H**, respectively. Forty-three cells in the perivascular invasion group and 40 cells in the intraparenchymal invasion group from three independent experiments were analyzed. Bars in the scatter-plot graphs indicate the means. P.V., perivascular invasion group; I.P., intraparenchymal invasion group. (**I**–**K**) A hypothetical model of glioblastoma progression. Scale bars: (A) 5 mm, (B–F) 100 μm. *P*-values were calculated using unpaired *t*-tests.

Journal of Cell Science

migrating along blood vessels (Fig. 1D, arrowhead; supplementary material Movie 1) and those invading the brain parenchyma (Fig. 1E; supplementary material Movie 2) exhibited striking differences, not only in their morphology but also in their mode of invasion. Glioblastoma cells migrating along blood vessels were spindle shaped with a single pseudopodium extending toward the direction of movement (Fig. 1D, arrowhead; supplementary material Movie 1), but glioblastoma cells invading the brain parenchyma extended multiple pseudopodia, which continuously probed in various directions (Fig. 1E; supplementary material Movie 2). One of these protrusions then became 'favored' and determined the direction of cell invasion; however the mechanisms underlying the selection of protrusion are not known. To quantify the difference in the two invasion modes, we measured the velocity and net displacement of the glioblastoma cells in each invasion mode at the periphery of the tumor mass (Fig. 1F). Both the velocity and net displacement of glioblastoma cells migrating along the perivascular region were larger than those of glioblastoma cells invading the parenchyma (Fig. 1G,H). These observations demonstrated two modes of glioblastoma invasion: (1) glioblastoma cells advance along blood vessels straightforwardly and rapidly (Fig. 1I); (2) some glioblastoma cells penetrate the brain parenchyma, extending multiple pseudopodia (Fig. 1J) eventually filling the inter-blood vessel space (Fig. 1K).

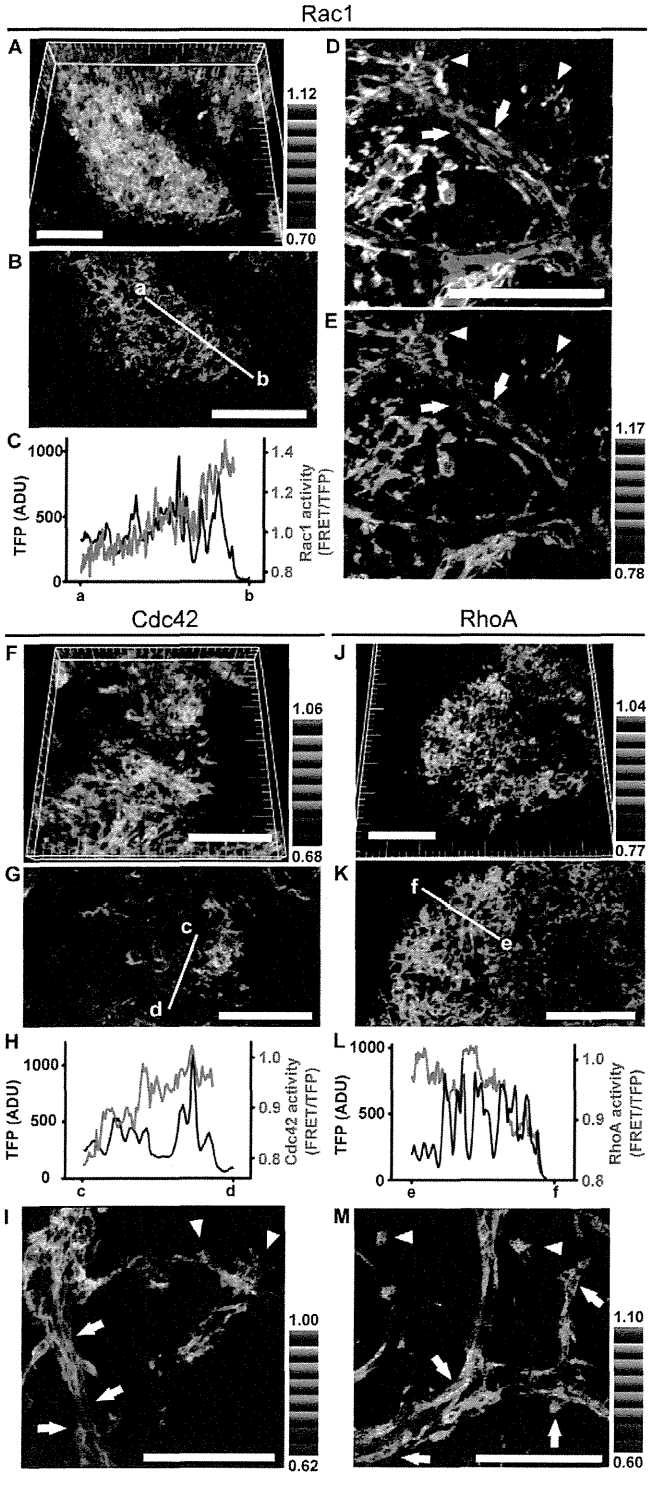

Glioblastoma cells invading the brain parenchyma showed higher Rac1 and Cdc42 activities and lower RhoA activity than those advancing in the perivascular region

To elucidate the role of Rho-family GTPases in the regulation of the two different invasion modes of glioblastoma cells, we developed new FRET biosensors that could be expressed stably in glioblastoma cells. For this purpose, we modified FRET biosensors for Rac1, Cdc42 and RhoA (Itoh et al., 2002; Yoshizaki et al., 2003) by adopting teal fluorescent protein (TFP) and a yellow fluorescent protein variant, Venus, as donor and acceptor fluorescent proteins, respectively (supplementary material Fig. S1). We found that the sensitivity and the dynamic rages of the new biosensors were almost comparable with those of the previously reported biosensors. Then, we established C6 glioblastoma cells stably expressing these biosensors, and grafted them into rat brains. Glioblastoma cells extending multiple pseudopodia at the periphery of the tumor mass grossly exhibited higher Rac1 activity than those inside the tumor mass (Fig. 2A–C), and this activity gradient was independent of the expression level of the biosensors (Fig. 2C). When viewed at higher magnification the glioblastoma cells invading the parenchyma with multiple pseudopodia (arrowheads in Fig. 2D,E) exhibited higher Rac1 activity than those

Fig. 2. Glioblastoma cells invading the brain parenchyma showed high Rac1 and Cdc42 activities. (**A–C**) C6 glioblastoma cells stably expressing the Raichu–Rac1 FRET biosensor were inoculated into rat brains, and the periphery of the tumor mass was imaged under a confocal laser scanning microscope, 7 days after inoculation. The three-dimensional reconstructed image (A) and representative section view (B) are shown in intensity-modulated display (IMD) mode with 32-intensity in 8-ratio. The gradient of the color bar shows the activity of Rac1 GTPase, with higher activity shown in red and lower activity in blue. The TFP intensity and Rac1 activity (FRET/TFP) on the section view in B was quantitatively analyzed by the line-scan method (a–b) and is shown in C. (**D,E**) An enlarged view around blood vessels from a similar experiment. The same section of glioblastoma cells is show in the mTFP channel with blood vessels in red (D) and Rac1 activity in the IMD mode (E). Images were constructed from the sum of three sequential images at 4 μm intervals. (**F–M**) C6 glioblastoma cells stably expressing Raichu–Cdc42 (F–I) or Raichu–RhoA (J–M) were analyzed using the same method. Scale bars: 100 μm.

Journal of Cell Science

Journal of Cell Science

advancing along blood vessels (arrows in Fig. 2D,E). A similar observation was obtained for Cdc42 (Fig. 2F–I). In clear contrast, RhoA activity was lower in the glioblastoma cells invading the parenchyma with multiple pseudopodia than in those advancing along blood vessels (Fig. 2J–M). To visualize the difference in the activities of Rho GTPases more clearly, we extracted Rac1-high (red) and Rac1-low (blue) signals from the IMD image (supplementary material Fig. S2B,F,J). We further quantified the FRET ratio by two methods. First, cells at the perivascular region and intraparenchymal region were marked manually and the FRET ratio (FRET/TFP) was calculated and compared (supplementary material Fig. S2C,D,G,H,K,L). Second, regions were automatically set depending on the distance from the blood vessels. The FRET ratio in each region was calculated and quantified (supplementary material Fig. S3). Both methods confirmed our observation that Rac1 and Cdc42 activities were lower and RhoA activity was higher at the perivascular region than at the intraparenchymal region, and vice versa. Although various artifacts should be taken into consideration in the intravital FRET imaging, this inverse correlation between the activities of Rac1 and Cdc42 and those of RhoA, partially ignores the possible artifacts caused by the difference in cell density, depth of tissue, etc. In short, these observations suggest two interesting possibilities. First, glioblastoma cells penetrating the parenchyma might be subjected to stimulants that activate Rac1 and Cdc42 but suppress RhoA. Second, each cell might stochastically exhibit a different level of Rho-family GTPase activities. In this scenario, cells with high Rac1 and Cdc42 but low RhoA activities penetrate the brain parenchyma, whereas cells with low Rac1 and Cdc42 but high RhoA activities persist to advance along the blood vessels.

Glioblastoma cells with higher Rac1 and Cdc42 activities guided the other glioblastoma cells with lower Rac1 and Cdc42 activities in a spheroid invasion assay

To test these two possibilities, we performed a 3D spheroid invasion assay (Gaggioli et al., 2007). C6 glioblastoma cells were cultured in suspension to form spheroids and embedded in 3D Matrigel. These C6 glioblastoma cells within the spheroid invaded into Matrigel in several directions (Fig. 3A). Interestingly, the glioblastoma cells with multiple pseudopodia led the other spindle-shaped cells during invasion (arrowheads and arrows in Fig. 3B, respectively). Magnified FRET imaging revealed that these glioblastoma cells leading the invasion had higher Rac1 activities (Fig. 3C–G; supplementary material Fig. S4 and Movie 3) and Cdc42 activities (Fig. 3H–K; supplementary material Fig. S4) than the trailing glioblastoma cells. By contrast, such intercellular divergence was not clear for RhoA activity (Fig. 3L–O; supplementary material Fig. S4). This pattern of activity gradient was similar to that found in the rat brain (Fig. 2), except that low RhoA activity in the multipod cells was not recapitulated in this spheroid invasion assay. Importantly, only a limited number of glioblastoma cells initiated the invasion of the gel, which should have been uniform in its concentration of growth factors. Therefore, these observations argue for the second hypothesis: namely, selected glioblastoma cells with higher Rac1 and Cdc42 activities invaded the gel, guiding those with lower Rac1 and Cdc42 activities. Under higher magnification, the activities of Rac1, Cdc42 and RhoA were all higher in the pseudopodia than in the cell bodies (Fig. 3P–R, respectively) as reported in conventional 2D culture dishes (Kurokawa and Matsuda, 2005). Thus, the failure to detect the intercellular divergence of RhoA activity was not due to the insensitivity of Raichu–RhoA under the 3D condition.

To verify the involvement of Rac1 and RhoA in formation of pseudopodia and invasion of gels, we performed a spheroid invasion assay in the presence of inhibitors of the Rac1 or RhoA pathway. NSC23766, which inhibits Rac1 activation, collapsed the pseudopodia and inhibited invasion of the gels (Fig. 3S, middle panel; supplementary material Movie 4). By contrast, Y27632, an inhibitor of the RhoA-dependent kinase ROCK, promoted the elongation of pseudopodia, which were thinner than those of the control cells. Notably, these pseudopodia could not accelerate the invasion (Fig. 3S, lower panel; supplementary material Movie 4). We examined the effect of NSC23766 and Y27632 on the global activities of RhoA, Rac1 and Cdc42 by pull-down analysis (supplementary material Fig. S5A). None of the Rho-family GTPases was inhibited by Y27632. NSC23766 inhibited only Rac1 activity, as expected. We also analyzed Rac1, Cdc42 and RhoA activities in the spheroid invasion assay in the presence of these inhibitors (supplementary material Fig. S5B). NSC23766 abolished glioblastoma invasion, concomitant with the global decrease in Rac1 activity. In the presence of NSC23766, the leading cells with high Cdc42 activity were lost; however, the Cdc42 activity was not altered in the central cell clusters. Y27632 did not affect the activities of RhoA, Rac1 or Cdc42. All these findings suggested that glioblastoma cells with higher Rac1 activity formed multiple pseudopodia and invaded the gel, guiding the other cells with lower Rac1 activity. The role of the RhoA–ROCK pathway was not clear in this assay.

Knockdown of Zizimin1 expression impeded formation of pseudopodia and invasion

We next looked for a guanine nucleotide exchange factor (GEF) that is responsible for the high Rac1 and Cdc42 activity in the invading glioblastoma cells with multiple pseudopodia. In preliminary shotgun transcriptome sequencing and microarray analyses, we identified GEFs for Rac1 and/or Cdc42 expressed in both C6 glioblastoma cells and human glioblastoma tissues. Among them, we focused on Zizimin1. Zizimin1 was originally identified as a Cdc42-specific GEF (Meller et al., 2002) and has been shown to regulate neurite outgrowth (Kuramoto et al., 2009). Because Cdc42 controls the formation of astrocytic processes and cell polarity in migrating astrocytes (Etienne-Manneville and Hall, 2001), and could activate Rac1 in a hierarchical manner (Nobes and Hall, 1995), Zizimin1 could cause the heterogeneity in Rac1 and/or Cdc42 activity and, thereby, the two glioblastoma invasion modes.

To investigate the possibility that Zizimin1 contributes to glioblastoma invasion, we developed C6 glioblastoma cells stably expressing three different shRNAs against rat Zizimin mRNA (Zizimin1 knockdown cells: Zizimin-KD-A, -B and -C) or control shRNA (Fig. 4A,B). A spheroid invasion assay revealed that Zizimin1 knockdown greatly inhibited the formation of pseudopodia and invasion of C6 glioblastoma cells (Fig. 4C; supplementary material Fig. S6 and Movie 5). Thus, we speculated that glioblastoma cells with high expression and/or activity of Zizimin1 exhibited high Rac1 and Cdc42 activities and guided the other glioblastoma cells. To test this possibility, C6 glioblastoma cells expressing shRNA and GFP were mixed with wild-type C6 glioblastoma cells expressing a red fluorescent protein, dKeima, to form spheroids, and embedded in

Journal of Cell Science

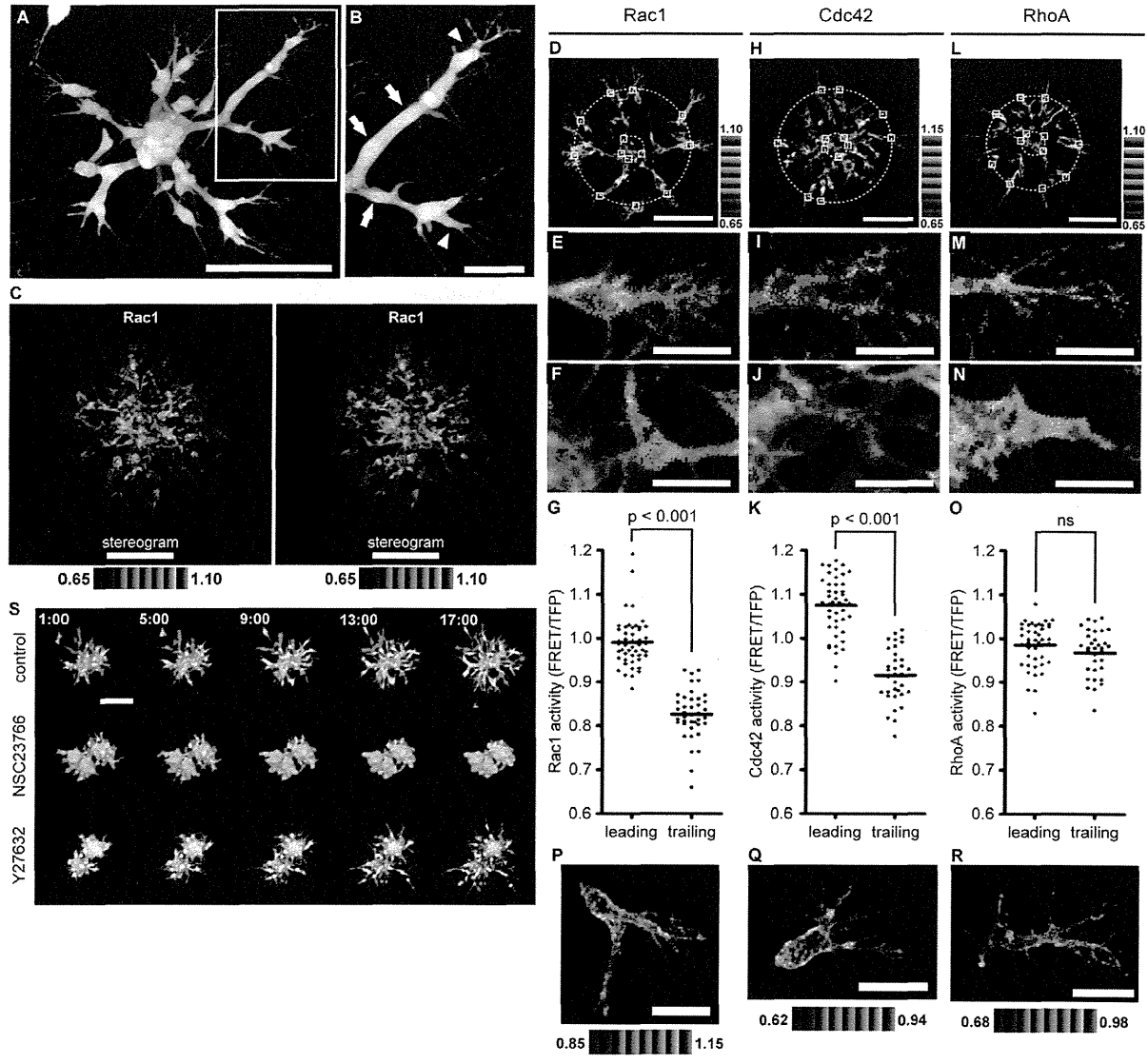

Fig. 3. High Rac1 activity was required for invasive multipod glioblastoma cells. (**A**,**B**) C6 glioblastoma cells stably expressing mEGFP were embedded in 6.0 mg/ml Matrigel and imaged under a confocal laser scanning microscope. The boxed region in A is magnified in B. (**C**) Spheroid invasion assay of C6 glioblastoma cells stably expressing the Raichu–Rac1 FRET biosensor. Cell clusters were imaged under a confocal laser scanning microscope 24 hours after being embedded in 3D Matrigel. The figures are shown in FRET IMD mode, and the two images form a stereogram for viewing by the cross-eyed method. (**D–O**) Cell clusters stably expressing Raichu–Rac1 (D), –Cdc42 (H) or –RhoA (I) were imaged and are shown in the same manner. To compare the activity (FRET/TFP ratio) of each Rho-family GTPase between cells leading invasion and cells trailing the leading cells, we set two concentric circles passing through the leading and trailing cells as shown in D,H,L. FRET images of representative cells on the outer (E,I,M) or inner circles (F,J,N) are magnified and shown. Then, square regions of interest (ROIs) of 8 by 8 pixels were set on the outer and inner circles. For each ROI, the FRET/TFP values were calculated and plotted (G,K,O). Bars in the scatter-plot graphs indicate the means. (**P–R**) FRET images focusing on the intracellular gradient of activity in Rac1 (P), Cdc42 (Q) and RhoA (R) are shown with different ratio ranges. (**S**) Spheroid invasion assay of C6 glioblastoma cells stably expressing mEGFP in the presence of the indicated reagent: NSC23766, a Rac1 inhibitor, Y27632, an inhibitor of the RhoA-dependent kinase ROCK. Image acquisition was started 1 hour after the addition of each regent. Scale bars: (A,C,D,H,L,S) 100 μm, (B,E,F,I,J,M,N,P–R) 30 μm. *P*-values were calculated using unpaired *t*-tests.

3D Matrigel. The C6 glioblastoma cells expressing the control shRNA and the wild-type C6 glioblastoma cells (green and red cells, respectively, in Fig. 4D and supplementary material Fig. S7 and Movie 6) were equally capable of forming multiple pseudopodia and invading the gel. By contrast, Ziziminl knockdown cells (green in Fig. 4E and supplementary material Fig. S7 and Movie 6) could not invade the gels at the front, but only trailed the preceding wild-type C6 glioblastoma cells (red in the same figures and movies).

We quantified the proportion of the control and Ziziminl knockdown cells in the leading cells in the spheroid assay (Fig. 4F). The C6 glioblastoma cells expressing the control shRNA accounted for 50% of leading cells, whereas Ziziminl knockdown cells accounted for approximately 20%. The velocities of wild-type and Ziziminl knockdown cells in the spheroid invasion assay were also measured for up to 16 hours (Fig. 4G,H). The wild-type C6 glioblastoma cells moved into the gels faster than the Ziziminl knockdown cells in the first 8 hours

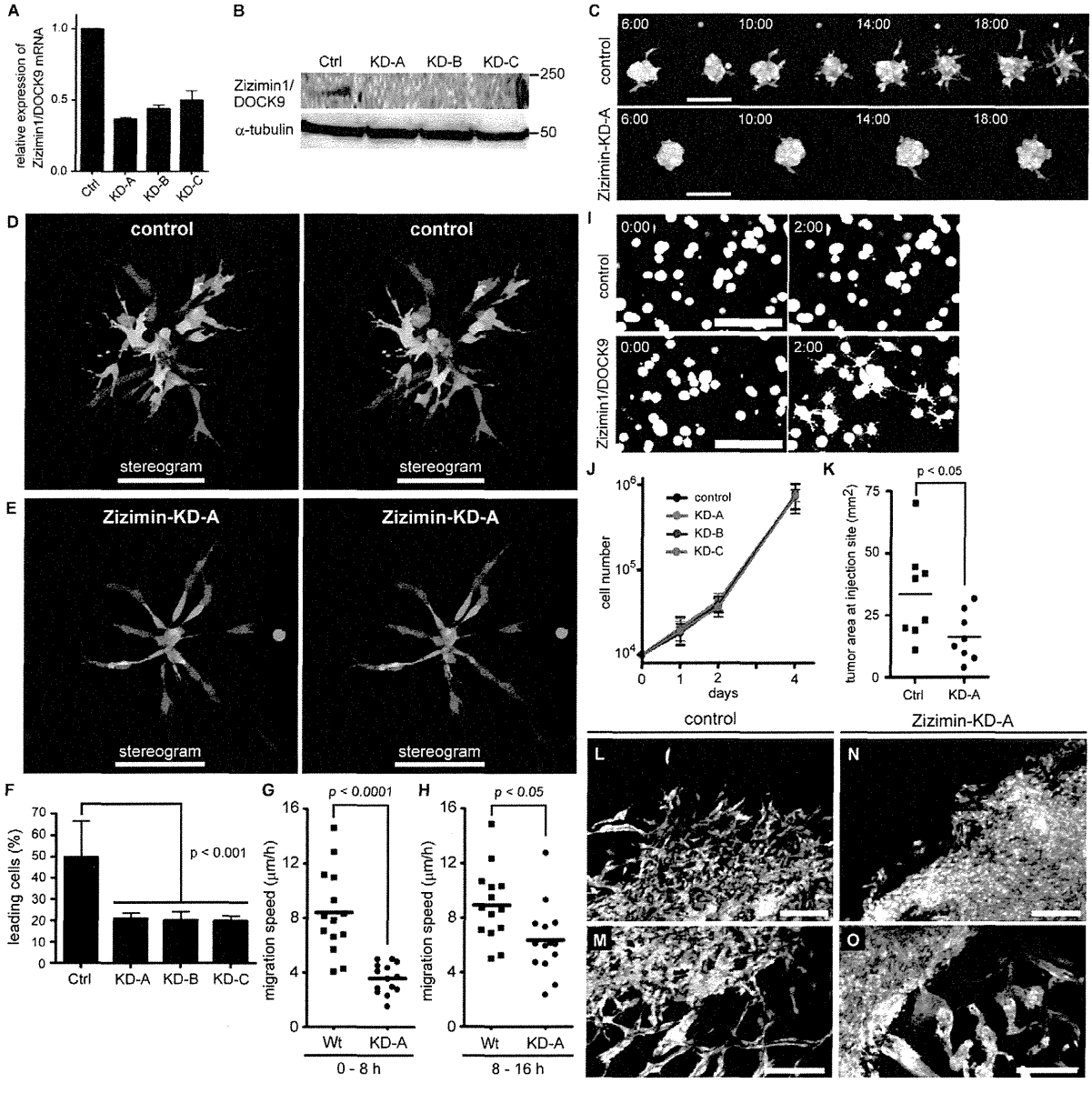

Fig. 4. Knockdown of Zizimin1 expression impeded formation of pseudopodia and invasion. (**A**,**B**) Three different shRNA-mediated RNA interference plasmids against rat Zizimin1 (Zizimin-KD-A, -B and -C) were introduced by retroviral vector into C6 glioblastoma cells stably expressing mEGFP. An shRNA targeting the firefly luciferase gene was used as a negative control. (A) The relative expression levels of Zizimin1 mRNA in the knockdown cells, as determined by quantitative RT-PCR. GAPDH was used as an internal control. Values are means ± s.d. (B) Cell lysates were subjected to SDS-PAGE and immunoblotting analysis with anti-Zizimin1 antibody and anti-α-tubulin antibody was used as a control. (**C**) Spheroid invasion assay of control (upper panel) and Zizimin1 knockdown (Zizimin-KD-A, lower panel) C6 glioblastoma cells stably expressing mEGFP in 3D Matrigel. Cell clusters were imaged under a confocal laser scanning microscope for up to 18 hours. (**D**–**H**) Control or Zizimin1 knockdown C6 glioblastoma cells stably expressing mEGFP were mixed with wild-type C6 glioblastoma cells stably expressing dKeima to form cell clusters, and embedded in 3D Matrigel. The cell clusters were imaged under a two-photon microscope 24 hours after being embedded in the gel. The two images each for D and E form a stereogram for viewing by the cross-eyed method. (F) The proportion of the control or Zizimin1 knockdown cells among the leading cells were calculated in nine independent spheroids, and are shown in a bar graph as means ± s.d. (G,H) Migration speed of wild-type C6 cells and Zizimin1 knockdown cells (Zizimin-KD-A) in the mixed spheroid invasion assay were measured in the first 8 hours (G) and in the second 8 hours (H). Each group of data consists of 14 cells from three independent experiments. Bars in the scatter-plot graphs indicate the means. (**I**) C6 glioblastoma cells stably expressing mEGFP were introduced with LDR (control; upper panels) or LDR and FKBP–Zizimin1–DHR2 (lower panels) by retroviral vector, and embedded into 3D Matrigel as single cells. The cells were treated with 50 nM rapamycin (at time 0:00) and imaged under a confocal laser scanning microscope for 2 hours. (**J**) The proliferation rates of control and Zizimin1 knockdown cells in vitro were calculated. Values are means ± s.d. (n=3). (**K**) Rat brains were inoculated with 5×10^5 control or Zizimin1 knockdown (Zizimin-KD-A) C6 glioblastoma cells, and the tumor size was analyzed 7 days after inoculation. The coronal section area at the injection site was taken as the tumor size. Bars in the scatter-plot graph indicate the means. (**L**–**O**) The peripheries of the tumor masses derived from control (H,I) or Zizimin1 knockdown (Zizimin-KD-A, J,K) C6 glioblastoma cells were imaged under a two-photon microscope. Scale bars: 100 μm. P-values were calculated using unpaired t-tests.

Journal of Cell Science

Journal of Cell Science

(Fig. 4G; supplementary material Movie 6); however, Zizimin1 knockdown cells were able to move into the gels by trailing the leading cells in the second 8 hours (Fig. 4H; supplementary material Movie 6). We examined whether the effect of shRNA could be cancelled by the expression of Zizimin1. The C6 glioblastoma cells stably expressing EGFP and shRNA against rat Zizimin1 were transfected with expression vectors of human Zizimin1 and histone-H1-conjugated mCherry, and subjected to the spheroid invasion assay (supplementary material Fig. S8). We found that 60% of the leading cells expressed the marker protein, mCherry, indicating that the effect of shRNA could be cancelled by the expression of human Zizimin1.

To further verify the role of Zizimin1 in the formation of pseudopodia in 3D gels, we developed C6 glioblastoma cells stably expressing the Lyn N-terminal sequence-tagged fragment of the mammalian target of rapamycin (LDR) and FK506 binding protein (FKBP)-fused Zizimin1 DHR2 domain (Inoue et al., 2005; Aoki et al., 2007). Rapamycin-induced membrane translocation of the DHR2 domain of Zizimin1 rapidly induced pseudopodia in C6 glioblastoma cells (Fig. 4I; supplementary material Movie 7), showing that Zizimin1 could play a pivotal role in the formation of pseudopodia through its GEF activity.

To examine whether Zizimin1 knockdown suppresses Rac1 and Cdc42 activities of C6 glioblastoma cells in the 3D spheroid invasion assay, we introduced control or Zizimin-KD-A shRNA into C6 glioblastoma cells stably expressing Raichu biosensors, and the Zizimin1 knockdown cells were marked with histone-H1-conjugated mCherry (supplementary material Fig. S9). The Zizimin1 knockdown cells were left behind and exhibited lower Rac1 and Cdc42 activities than the control cells leading the invasion. These findings suggest that Zizimin1 promotes formation of pseudopodia and concomitant invasion of C6 glioblastoma cells through Cdc42 activation in the 3D Matrigel condition.

Next, to investigate the role of Zizimin1 in glioblastoma progression in vivo, we inoculated rat brains with control or Zizimin1 knockdown glioblastoma cells. Although the Zizimin1 knockdown cells replicated as efficiently as the control cells in the culture dish (Fig. 4J), the Zizimin1 knockdown cells ostensibly grew more slowly than the control cells in brain tissues (Fig. 4K). Histologically, the control glioblastoma cells diffusely invaded the brain tissue from the perivascular region (Fig. 4L,M), whereas Zizimin1 knockdown glioblastoma cells were well demarcated from the surrounding brain tissues (Fig. 4N) and packed densely around the perivascular region (Fig. 4O). These results suggested that formation of pseudopodia by Zizimin1 was required for C6 glioblastoma cell progression in vivo, and that Zizimin1 drove glioblastoma cells around the perivascular region to invade the brain parenchyma.

Human glioblastoma cell lines also exhibited the gradient of Rac1 and Cdc42 activities and dependency on Zizimin1

To investigate whether human glioblastoma cells also exhibited a gradient of Rho-family GTPase activity during invasion of the gel, we introduced Raichu biosensors into three human glioblastoma cell lines, U251MG, LN229 and U87MG, and performed the 3D spheroid invasion assay (Fig. 5A–C). FRET microscopy revealed that cells leading the invasion exhibited higher Rac1 and Cdc42 activity than the trailing cells in all human glioblastoma cell lines. However, the intercellular gradient for RhoA activity varied depending on the cell type. The leading U251MG cells had slightly higher RhoA activity than the trailing cells (Fig. 5A); the gradient was not clear in LN229 cells (Fig. 5B); and in U87MG cells the RhoA activity of the leading cells was lower than that of the trailing cells (Fig. 5C). These findings suggest that the human glioblastoma cells with higher Rac1 and Cdc42 activity guide the other human glioblastoma cells with lower Rac1 and Cdc42 activity, as in rat C6 glioblastoma cells, and that RhoA activity might play different roles depending on the glioblastoma cells.

Next, to investigate whether Zizimin1 played an important role in human glioblastoma cell invasion as in rat C6 glioblastoma cells, we established human glioblastoma cells stably-expressing shRNA against human Zizimin1 mRNA (Fig. 5D,E). Knockdown of Zizimin1 in U251MG cells did not have any effect in the 3D spheroid invasion assay (Fig. 5F, upper panels). However, knockdown of Zizimin1 in LN229 and U87MG cells impeded formation of pseudopodia and invasion of the gel (Fig. 5G,H, respectively, upper panels). To reconstitute in vivo human glioblastoma tissue consisting of cells with various expression and/or activity levels of Zizimin1, glioblastoma cells with or without Zizimin1 shRNA were mixed to form spheroids, and a 3D invasion assay was performed. We found that Zizimin1 knockdown LN229 or U87MG cells could only follow the wild-type glioblastoma cells into the gels (Fig. 5G,H, respectively, lower panels). Again, we could not find any effect of Zizimin1 shRNA in U251MG cells (Fig. 5F, lower panels). These findings indicate that Zizimin1 also plays a pivotal role in formation of pseudopodia and invasion in some human glioblastoma cells, as in rat C6 glioblastoma cells.

Discussion

Previous histological studies have shown that C6 glioblastoma cells invade through the perivascular space and along neuronal fibers of the brain parenchyma, as do the genuine human glioblastoma cells (Grobben et al., 2002). Ex vivo time-lapse images taken with conventional fluorescence microscopy have further highlighted the importance of the perivascular growth of C6 glioblastoma cells (Farin et al., 2006). Recently, Winkler et al. used a two-photon microscope to observe the invasion of mouse glioblastoma cells and reported that the perivascular glioblastoma cells moved faster than did the glioblastoma cells in the parenchyma (Winkler et al., 2009). We also confirmed these findings for C6 glioblastoma cells by using a two-photon microscope, and further demonstrated that glioblastoma cells exhibited two distinct modes of invasion depending on whether they were located in the perivascular region or parenchyma (Fig. 1). Glioblastoma cells migrating in the perivascular region had an elongated spindle shape that is consistent with mesenchymal migration (Friedl and Wolf, 2010). By contrast, most of the glioblastoma cells in the brain parenchyma resembled normal astrocytes. Interestingly, time-lapse microscopy revealed that some glioblastoma cells dynamically changed their invasion paths from the perivascular region to the intraparenchymal region, and vice versa. These findings motivated us to examine the mechanistic aspect of the switch between the two invasive modes of glioblastoma, because flexible alteration of the two invasion modes in individual glioblastoma cells could lead to effective progression of glioblastomas.

FRET imaging demonstrated that glioblastoma cells extending multiple pseudopodia at the invasion front exhibited higher Rac1 and Cdc42 activities and lower RhoA activity compared with

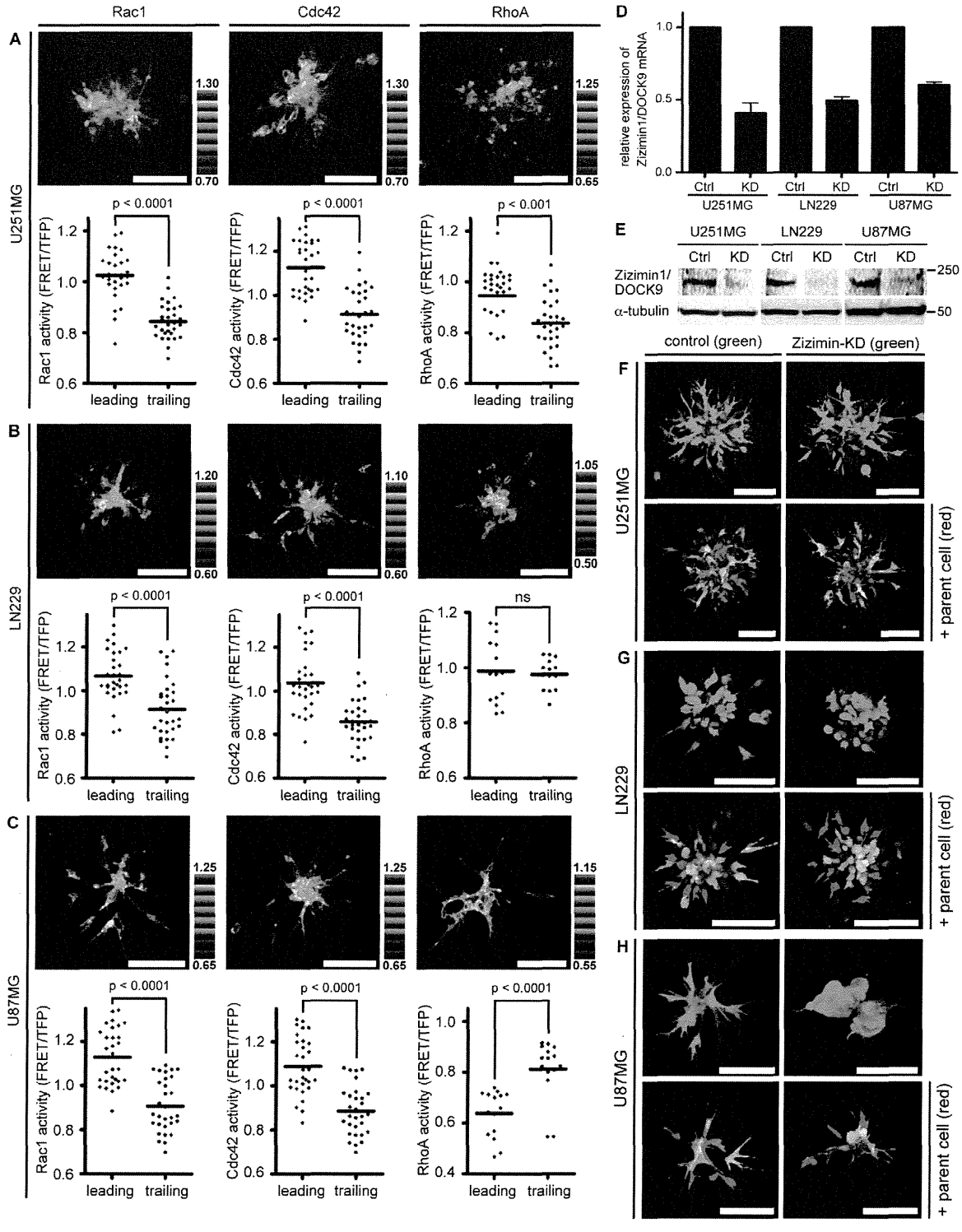

Fig. 5. Rac1 and Cdc42 activity and Zizimin1 expression in human glioblastoma correlated with their invasiveness in 3D culture. (**A–C**) Three human glioblastoma cells lines, U251MG, LN229 and U87MG, stably expressing the Raichu–Rac1, –Cdc42 and –RhoA were established and subjected to the spheroid invasion assay. Cell clusters were imaged under a confocal laser scanning microscope 36 hours (U251MG and LN229MG) or 18 hours (U87MG) after being embedded in 3D Matrigel. The activities of each GTPase are depicted in FRET IMD mode and were analyzed quantitatively as in Fig. 3. Bars in the scatter plots indicate the means. (**D**,**E**) An shRNA-mediated RNA interference plasmid against human Zizimin1 was introduced by a retroviral vector into three human glioblastoma cell lines stably expressing mEGFP. An shRNA targeting firefly luciferase transcription was used as a negative control. (D) The relative expression levels of Zizimin1 mRNA in knockdown cells as determined by quantitative RT-PCR. GAPDH was used as an internal control. Values are means ± s.d. (E) The protein expression level was examined by western blotting as in Fig. 3B. (**F–H**) Spheroid invasion assay of control and Zizimin1 knockdown cells (upper panels). Cell clusters were imaged under a confocal laser scanning microscope 36 hours (U251MG and LN229MG) or 18 hours (U87MG) after being embedded in 3D Matrigel. In other experiments (lower panels), shRNA-carrying cells labeled with GFP were mixed with the parent cells labeled with dKeima to form cell clusters, and embedded in 3D Matrigel. The cell clusters were imaged under a two-photon microscope 36 hours (U251MG and LN229MG) or 18 hours (U87MG) after being embedded in the gel. Scale bars: 100 μm. *P*-values were calculated using unpaired *t*-tests.

Journal of Cell Science

Journal of Cell Science

glioblastoma cells at the perivascular region (Fig. 2). To the best of our knowledge, this is the first report to show the intercellular activity gradient of small GTPases in living cancer tissues, although previous studies using inhibitors and mutants have suggested that the differential use of Rho-family GTPases determines the mode of cancer cell invasion (Sahai and Marshall, 2003; Sanz-Moreno et al., 2008; Yamazaki et al., 2009; Friedl and Wolf, 2010). The gradient of Rho-family GTPase activity within the glioblastoma tissue strongly supports the idea that the two glioblastoma invasion modes are correlated with the activities of Rho-family GTPases. Interestingly, recent studies by Panopoulos et al. showed that mesenchymal migration of glioblastoma cells does not require Rac1 activity on 2D substrates (Panopoulos et al., 2011). This observation suggests that glioblastoma cells do not require Rac1 activity to move without marked resistance on dishes or around blood vessels. At the same time, our observations suggested two scenarios for the increased Rac1 and Cdc42 activities: high activities of Rac1 and Cdc42 might be induced within cells invading the brain parenchyma, or cells with high Rac1 and Cdc42 activities might be driven from the perivascular space into the parenchyma.

Three lines of evidence from the 3D invasion assay support the second scenario, i.e. C6 glioblastoma cells with high Rac1 and Cdc42 activities preferentially invade the parenchyma. First, we found that C6 glioblastoma cells with high Rac1 and Cdc42 activities guided the other cells to invade the gel (Fig. 3; supplementary material Fig. S4). Second, inhibition of Rac1 activity by NSC23766 reduced the size and number of pseudopodia and suppressed the invasion (Fig. 3S; supplementary material Movie 4). We confirmed this observation with C6 glioblastoma cells expressing a dominant-negative mutant of Rac1 (data not shown). Third, Zizimin1 knockdown decreased the Rac1 and Cdc42 activities, reduced the number of cellular protrusions in C6 glioblastoma cells and suppressed the invasion in 3D Matrigel cultures (Fig. 4; supplementary material Figs S7 and S9). Intriguingly, cells with reduced Zizimin1 expression could follow the wild-type C6 glioblastoma cells in 3D culture, indicating that high Cdc42 activity is required for the invasion of the gel but not for the migration itself (Fig. 4G,H; supplementary material Movie 6).

We previously reported that Rac1 and Cdc42 activities are high in lamellipodia (Itoh et al., 2002). Thus, cells with multiple pseudopodia could contribute to high Rac1 and Cdc42 activities in cells at the invasion front. However, as shown in the magnified FRET images (Fig. 3), the leading cells exhibited high Rac1 and Cdc42 activities not only in the pseudopodia but also in the cell bodies, in comparison with the trailing cells. Thus, we concluded that the high Rac1 and Cdc42 activities in the leading cells were not caused by the presence of multiple pseudopodia.

The relevance of our finding to the development of human glioblastoma is partially validated by the use of human glioblastoma cell lines. We found that invasion-leading cells exhibited higher Rac1 and Cdc42 activity than the trailing cells in human glioblastoma cells (Fig. 5A–C), as in rat C6 glioblastoma cells, and that knockdown of Zizimin1 in LN229 and U87MG cells impeded cell invasion of the gel (Fig. 5G,H). Because knockdown of Zizimin1 in U251MG cells did not alter the invasive phenotype, we consider that the contribution of Zizimin1 to glioblastoma cell invasion might be cell-type dependent. In fact, C6, LN229 and U87MG cells expressing shRNA against Zizimin1 were found to still be capable of invading the gel when examined for longer times (data not shown), suggesting that there are other molecules cooperating with or substituting for Zizimin1. Notably, using fluorescence-based cell sorting analysis and a pull-down assay (data not shown), knockdown of Zizimin1 was not found to affect the activities of Rac1 and Cdc42 in the C6 glioblastoma cells grown on culture dishes. This observation strongly suggests that the role played by Zizimin1 is specific to the glioblastoma cells growing in 3D conditions. In addition, although Zizimin1 is highly expressed in brain (Meller et al., 2002), we found that it is not upregulated in human glioblastoma cells compared with normal brain tissue (data not shown). To the best of our knowledge, there is no previous report showing a positive or negative correlation between the Zizimin1 mRNA expression level and cell proliferation, cell invasion or the prognosis of glioblastoma patients (Phillips et al., 2006; Shirahata et al., 2007). Therefore, we could speculate that Zizimin1 might be regulated primarily by the protein activity rather than by the gene expression in glioblastoma cells and that a glioblastoma cell population should contain a small fraction of cells with high Zizimin1 activity that is highly invasive in brain parenchyma. Actually, in our observations of rat brain, only a small number of glioblastoma cells produced multiple pseudopodia and penetrated brain parenchyma (Fig. 1), as was reported in a previous study in which only a small fraction (~5%) of cancer cells showed high invasiveness in vivo (Giampieri et al., 2009).

In summary, we demonstrated that invasion modes of glioblastoma cells can be controlled by the balance of the activity of Rho-family GTPases and a Cdc42-specific GEF, and Zizimin1 appears to play an important role in the formation of multiple pseudopodia and in invasion of the brain parenchyma. Our results provide further information about the nature of heterogeneity in cancer cell populations that are composed of various cells with different fingerprints of invasiveness.

Materials and Methods

Probes and cell lines

C6 rat glioblastoma cells, U251MG, LN229 and U87MG human glioblastoma cells, and Cos7 African green monkey SV40-transformed kidney fibroblast cells were obtained from the American Type Culture Collection and cultured in DMEM containing 10% FBS. The prototype FRET biosensors for Rac1, RhoA and Cdc42 were described previously (Itoh et al., 2002; Yoshizaki et al., 2003). In the Raichu–Rac1 biosensor (2227x), Raichu–Cdc42 biosensor (2219x) and Raichu–RhoA biosensor (1523x) used in this study, CFP was replaced with the teal fluorescent protein as described previously (Yoshiki et al., 2010). A pCX4 retroviral vector was used to express the FRET biosensors and fluorescent proteins in each glioblastoma cell line as described previously (Takaya et al., 2007). The infected cells were single-cell cloned before further experiments unless described otherwise.

Intracranial transplantation of glioblastoma cells and brain slice culture

All animal care measures and experiments complied with Japanese community standards on the care and use of laboratory animals, which were approved by Kyoto University. C6 glioblastoma cells (5×10^5 cells/5 μl PBS) were stereotactically transplanted into the right subcortex of 3-week-old male Wistar rats. After 7 days, tumor-bearing rats were killed with carbon dioxide and sodium pentobarbital, and decapitated. In preliminary experiments, Texas-Red-conjugated dextran (70 kDa; Invitrogen, Carlsbad, CA) was injected into the left ventricle before decapitation to visualize blood vessels; however, we omitted this process in later experiments because we could easily distinguish blood vessels by the morphologies and distribution of cells at invasion borders. The whole brains were quickly removed, cut vertically and mounted on the stage of a Vibroslice Tissue Cutter (Campden Instruments, Loughborough, UK) filled with ice-cold artificial cerebrospinal fluid containing 135 mM *N*-methyl-D-glucamine, 1 mM KCl, 1.2 mM KH_2PO_4, 20 mM choline bicarbonate, 10 mM glucose, 1.5 mM $MgCl_2$ and 0.5 mM $CaCl_2$. Coronal brain slices (300 μm thick) were cut and transferred onto a plastic coverslip and incubated in slice culture medium at 37°C in a humidified atmosphere containing 5% CO_2 as described previously (Tanaka et al.,

Journal of Cell Science

2008). The slice culture medium consisted of 77% MEM, 20% HBSS, 3% HEPES, 6.5 mg/ml glucose, 6.5 mg/ml L-glutamine and N2 supplement (all from Invitrogen). For tumor size calculation, brain samples were prepared by perfusion fixation. A coronal section at the injection site was prepared for each sample and imaged under a fluorescence stereomicroscope (Carl Zeiss Meditec Inc., Dublin, CA).

Two-photon excitation microscopy and confocal laser scanning microscopy

Cultured brain slices were maintained in an incubation chamber (Tokai Hit, Shizuoka, JAPAN) and imaged using a 20× water-immersion objective (XLUMPLFL20; Olympus Optical Co., Tokyo, Japan) on a BX61WI/FV1000 upright microscope (Olympus) equipped with a 440 nm laser diode (Olympus) and a Mai-Tai Ti:sapphire laser (Spectra Physics, Mountain View, CA). The excitation wavelength for two-photon excitation was 850 nm. We used a RDM650 IR-cut filter, a DM570 dichroic mirror and two emission filters: BA510-550 for GFP and BA570-625 for Keima or Texas Red, respectively. All filters were purchased from Olympus. For FRET imaging with a confocal laser scanning unit, we used a 440 nm laser diode and the following filter sets purchased from Olympus: an excitation dichroic mirror, DM405-440/515, a second dichroic mirror, SDM510, and two emission filters, BA465-495 for TFP and BA520-550 for FRET. To obtain the intensity profile of the Raichu biosensors, we used the FV1000 lambda-scan program with a 440 nm laser diode and a beam splitter BS/20/80 (Olympus), and an SPD (Olympus) emission detecting system. Fluorescence intensities at every 5 nm wavelength with 10 nm bandwidth were obtained from 470 nm to 550 nm.

Image processing

Acquired images were analyzed with MetaMorph software (Universal Imaging, West Chester, PA). For 3D reconstruction of the images and calculation of the cell migration speed in a 3D environment, the original confocal images were analyzed with Imaris Software (Bitplane AG, Zürich, Switzerland). The tumor area was calculated according to the fluorescence signal with MetaMorph software.

Invasion assays

The organotypic culture system was set up as previously described (Gaggioli et al., 2007). Briefly, cells were embedded in Matrigel (BD Biosciences, Bedford, MA) at a concentration of approximately 6 mg/ml. For spheroid invasion assays, 1×10^6 cells in 1 ml serum-free CO_2-independent medium (Invitrogen) were agitated overnight in a 12-well plate coated with poly(2-hydroxyethyl methacrylate) (Sigma, St. Louis, MO) to form small aggregates. The aggregates were embedded in Matrigel, maintained in complete medium and observed under a two-photon or a confocal microscope for up to 18 hours in an incubation chamber. Y27632 and NSC23766 were obtained from Calbiochem (La Jolla, CA) and used at final concentrations of 20 μM and 100 μM, respectively.

shRNA-mediated knockdown of Zizimin1 and quantitative RT-PCR

pSuper.retro.puro vector (OligoEngine, Seattle, WA) was used for the expression of short hairpin RNA (shRNA). shRNAs for rat Zizimin1 were kind gifts from Hironori Katoh, Graduate School of Biostudies, Kyoto University (Kuramoto et al., 2009). An shRNA for human Zizimin1 (5′-TGGTTCCGGTTTAGATAGCTA-3′) was obtained from the Genome Network Project at the University of Tokyo (http://gnp.rnai.jp/). shRNA targeting firefly luciferase transcription (5′-GATTATGTCCGGTTATGTA-3′) was used as a negative control. The efficiency of knockdown was determined by quantitative RT-PCR. Second-derivative maximum method was applied for crossing-point determination using LightCycler version 3.3 software (Roche, Basel, Switzerland) (Hirata et al., 2009). GAPDH was used as an internal control. The following primer sets were used: for rat Zizimin1, forward 5′-CATGCAGGATGTCCATTTCA-3′, and reverse 5′-CGTGTCATACAGGTGGGCTA-3′; for rat *GAPDH*, forward 5′-GAGTC-TACTGGCGTCTTCAC-3′, and reverse 5′-GTTCACACCCATCACAAACA-3′; for human Zizimin1, forward 5′-TCCGTGTAGTGTGCAACCAT-3′, and reverse 5′-CAGTCCCACCAAGAAGTGGT-3′; for human *GAPDH*, forward 5′-GAGTCCACTGGCGTCTTCAC-3′, and reverse 5′-GTTCACACCCATGACG-AACA-3′. The conditions for PCR were 45 cycles of 95℃ for 10 seconds for denaturation, 56℃ for 10 seconds for annealing and 72℃ for 10 seconds for extension.

Pull-down assay and immunoblotting

The activities of Rac1, Cdc42 and RhoA in C6 glioblastoma cells were measured by the Bos' pull-down method (Aoki et al., 2005). Briefly, cells were harvested in ice-cold lysis buffer (50 mM Tris, pH 7.5, 100 mM NaCl, 2 mM $MgCl_2$, 1% Nonidet P-40, 10% glycerol, 1 mM dithiothreitol) containing GST–PAK–CRIB for Rac1 and Cdc42 or Rhotekin–RBD for RhoA. The cleared lysates were incubated with glutathione–Sepharose beads for 30 minutes at 4℃. The washed beads were boiled in sample buffer, and both the bound proteins and total cell lysates were analyzed by SDS-PAGE followed by immunoblotting. Precast SDS–polyacrylamide gels were purchased from Wako Pure Chemical Industries (Tokyo, Japan). Bound antibodies were detected with secondary antibodies conjugated with IRDye680 or IRDye800 and analyzed with an Odyssey Imager system (LICOR, Lincoln, NE). Anti-Rac1 and anti-Cdc42 mouse monoclonal antibodies were purchased from BD Transduction Laboratory (San Diego, CA). Anti-RhoA mouse monoclonal antibody was purchased from Santa Cruz Biotechnology (Santa Cruz, CA). Anti-human DOCK9 mouse monoclonal antibody was a kind gift from Martin A. Schwartz (Yale University) and anti α-tubulin mouse monoclonal antibody was purchased from Calbiochem.

Statistical analysis

When two groups were compared, a two-tailed unpaired Student's *t*-test was applied.

Acknowledgements

We thank H. Katoh, A. Miyawaki, T. Akagi, J. Miyazaki and M. A. Schwartz for the plasmids and antibodies. Y. Inaoka, K. Hirano, R. Sakai and N. Nonaka are also to be thanked for their technical assistance. We are grateful to the members of the Matsuda Laboratory for their helpful discussions.

Funding

This work was supported by a Sagawa Cancer Research Grant [awarded in 2008 to M.M.]; the Research Program of Innovative Cell Biology by Innovative Technology (Cell Innovation) from the Ministry of Education, Culture, Sports and Science (MEXT), Japan to M.M.; and the Global Center of Excellence Program "Center for Frontier Medicine" initiated by Ministry of Education, Culture, Sports and Science, Japan.

Supplementary material available online at
http://jcs.biologists.org/lookup/suppl/doi:10.1242/jcs.089995/-/DC1

References

Aoki, K. and Matsuda, M. (2009). Visualization of small GTPase activity with fluorescence resonance energy transfer-based biosensors. *Nat. Protoc.* **4**, 1623-1631.

Aoki, K., Nakamura, T., Fujikawa, K. and Matsuda, M. (2005). Local phosphatidylinositol 3,4,5-trisphosphate accumulation recruits Vav2 and Vav3 to activate Rac1/Cdc42 and initiate neurite outgrowth in nerve growth factor-stimulated PC12 cells. *Mol. Biol. Cell* **16**, 2207-2217.

Aoki, K., Nakamura, T., Inoue, T., Meyer, T. and Matsuda, M. (2007). An essential role for the SHIP2-dependent negative feedback loop in neuritogenesis of nerve growth factor-stimulated PC12 cells. *J. Cell Biol.* **177**, 817-827.

Bellail, A. C., Hunter, S. B., Brat, D. J., Tan, C. and Van Meir, E. G. (2004). Microregional extracellular matrix heterogeneity in brain modulates glioma cell invasion. *Int. J. Biochem. Cell Biol.* **36**, 1046-1069.

Croft, D. R. and Olson, M. F. (2008). Regulating the conversion between rounded and elongated modes of cancer cell movement. *Cancer Cell* **14**, 349-351.

Etienne-Manneville, S. and Hall, A. (2001). Integrin-mediated activation of Cdc42 controls cell polarity in migrating astrocytes through PKCzeta. *Cell* **106**, 489-498.

Farin, A., Suzuki, S. O., Weiker, M., Goldman, J. E., Bruce, J. N. and Canoll, P. (2006). Transplanted glioma cells migrate and proliferate on host brain vasculature: a dynamic analysis. *Glia* **53**, 799-808.

Friedl, P. and Wolf, K. (2010). Plasticity of cell migration: a multiscale tuning model. *J. Cell Biol.* **188**, 11-19.

Furnari, F. B., Fenton, T., Bachoo, R. M., Mukasa, A., Stommel, J. M., Stegh, A., Hahn, W. C., Ligon, K. L., Louis, D. N., Brennan, C. et al. (2007). Malignant astrocytic glioma: genetics, biology, and paths to treatment. *Genes Dev.* **21**, 2683-2710.

Gaggioli, C., Hooper, S., Hidalgo-Carcedo, C., Grosse, R., Marshall, J. F., Harrington, K. and Sahai, E. (2007). Fibroblast-led collective invasion of carcinoma cells with differing roles for RhoGTPases in leading and following cells. *Nat. Cell Biol.* **9**, 1392-1400.

Giampieri, S., Manning, C., Hooper, S., Jones, L., Hill, C. S. and Sahai, E. (2009). Localized and reversible TGFbeta signalling switches breast cancer cells from cohesive to single cell motility. *Nat. Cell Biol.* **11**, 1287-1296.

Grobben, B., De Deyn, P. P. and Slegers, H. (2002). Rat C6 glioma as experimental model system for the study of glioblastoma growth and invasion. *Cell Tissue Res.* **310**, 257-270.

Hirata, E., Arakawa, Y., Shirahata, M., Yamaguchi, M., Kishi, Y., Okada, T., Takahashi, J. A., Matsuda, M. and Hashimoto, N. (2009). Endogenous tenascin-C enhances glioblastoma invasion with reactive change of surrounding brain tissue. *Cancer Sci.* **100**, 1451-1459.

Inoue, T., Heo, W. D., Grimley, J. S., Wandless, T. J. and Meyer, T. (2005). An inducible translocation strategy to rapidly activate and inhibit small GTPase signaling pathways. *Nat. Methods* **2**, 415-418.

Itoh, R. E., Kurokawa, K., Ohba, Y., Yoshizaki, H., Mochizuki, N. and Matsuda, M. (2002). Activation of rac and cdc42 video imaged by fluorescent resonance energy

transfer-based single-molecule probes in the membrane of living cells. *Mol. Cell. Biol.* **22**, 6582-6591.

Kamiyama, D. and Chiba, A. (2009). Endogenous activation patterns of Cdc42 GTPase within Drosophila embryos. *Science* **324**, 1338-1340.

Kuramoto, K., Negishi, M. and Katoh, H. (2009). Regulation of dendrite growth by the Cdc42 activator Zizimin1/Dock9 in hippocampal neurons. *J. Neurosci. Res.* **87**, 1794-1805.

Kurokawa, K. and Matsuda, M. (2005). Localized RhoA activation as a requirement for the induction of membrane ruffling. *Mol. Biol. Cell* **16**, 4294-4303.

Louis, D. N., Ohgaki, H., Weistler, O. D. and Cavenee, W. K. (2007). *WHO Classification of Tumours of the Central Nervous System*. Switzlerland: World Health Organization Press.

Machacek, M., Hodgson, L., Welch, C., Elliott, H., Pertz, O., Nalbant, P., Abell, A., Johnson, G. L., Hahn, K. M. and Danuser, G. (2009). Coordination of Rho GTPase activities during cell protrusion. *Nature* **461**, 99-103.

Meller, N., Irani-Tehrani, M., Kiosses, W. B., Del Pozo, M. A. and Schwartz, M. A. (2002). Zizimin1, a novel Cdc42 activator, reveals a new GEF domain for Rho proteins. *Nat. Cell Biol.* **4**, 639-647.

Miyagi, C., Yamashita, S., Ohba, Y., Yoshizaki, H., Matsuda, M. and Hirano, T. (2004). STAT3 noncell-autonomously controls planar cell polarity during zebrafish convergence and extension. *J. Cell Biol.* **166**, 975-981.

Nobes, C. D. and Hall, A. (1995). Rho, rac, and cdc42 GTPases regulate the assembly of multimolecular focal complexes associated with actin stress fibers, lamellipodia, and filopodia. *Cell* **81**, 53-62.

Panopoulos, A., Howell, M., Fotedar, R. and Margolis, R. L. (2011). Glioblastoma motility occurs in the absence of actin polymer. *Mol. Biol. Cell* **22**, 2212-2220.

Pertz, O., Hodgson, L., Klemke, R. L. and Hahn, K. M. (2006). Spatiotemporal dynamics of RhoA activity in migrating cells. *Nature* **440**, 1069-1072.

Phillips, H. S., Kharbanda, S., Chen, R., Forrest, W. F., Soriano, R. H., Wu, T. D., Misra, A., Nigro, J. M., Colman, H., Soroceanu, L. et al. (2006). Molecular subclasses of high-grade glioma predict prognosis, delineate a pattern of disease progression, and resemble stages in neurogenesis. *Cancer Cell* **9**, 157-173.

Sahai, E. and Marshall, C. J. (2003). Differing modes of tumour cell invasion have distinct requirements for Rho/ROCK signalling and extracellular proteolysis. *Nat. Cell Biol.* **5**, 711-719.

Sahai, E., Garcia-Medina, R., Pouyssegur, J. and Vial, E. (2007). Smurf1 regulates tumor cell plasticity and motility through degradation of RhoA leading to localized inhibition of contractility. *J. Cell Biol.* **176**, 35-42.

Sanz-Moreno, V., Gadea, G., Ahn, J., Paterson, H., Marra, P., Pinner, S., Sahai, E. and Marshall, C. J. (2008). Rac activation and inactivation control plasticity of tumor cell movement. *Cell* **135**, 510-523.

Shirahata, M., Iwao-Koizumi, K., Saito, S., Ueno, N., Oda, M., Hashimoto, N., Takahashi, J. A. and Kato, K. (2007). Gene expression-based molecular diagnostic system for malignant gliomas is superior to histological diagnosis. *Clin. Cancer Res.* **13**, 7341-7356.

Takaya, A., Kamio, T., Masuda, M., Mochizuki, N., Sawa, H., Sato, M., Nagashima, K., Mizutani, A., Matsuno, A., Kiyokawa, E. et al. (2007). R-Ras regulates exocytosis by Rgl2/Rlf-mediated activation of RalA on endosomes. *Mol. Biol. Cell* **18**, 1850-1860.

Tanaka, Y., Tanaka, Y. Furuta, T., Yanagawa, Y. and Kaneko, T. (2008). The effects of cutting solutions on the viability of GABAergic interneurons in cerebral cortical slices of adult mice. *J. Neurosci. Methods* **171**, 118-125.

Winkler, F., Kienast, Y., Fuhrmann, M., Von Baumgarten, L., Burgold, S., Mitteregger, G., Kretzschmar, H. and Herms, J. (2009). Imaging glioma cell invasion in vivo reveals mechanisms of dissemination and peritumoral angiogenesis. *Glia* **57**, 1306-1315.

Yamazaki, D., Kurisu, S. and Takenawa, T. (2009). Involvement of Rac and Rho signaling in cancer cell motility in 3D substrates. *Oncogene* **28**, 1570-1583.

Yoshiki, S., Matsunaga-Udagawa, R., Aoki, K., Kamioka, Y., Kiyokawa, E. and Matsuda, M. (2010). Ras and calcium signaling pathways converge at Raf1 via the Shoc2 scaffold protein. *Mol. Biol. Cell* **21**, 1088-1096.

Yoshizaki, H., Ohba, Y., Kurokawa, K., Itoh, R. E., Nakamura, T., Mochizuki, N., Nagashima, K. and Matsuda, M. (2003). Activity of Rho-family GTPases during cell division as visualized with FRET-based probes. *J. Cell Biol.* **162**, 223-232.

Journal of Cell Science

SCIENTIFIC REPORTS

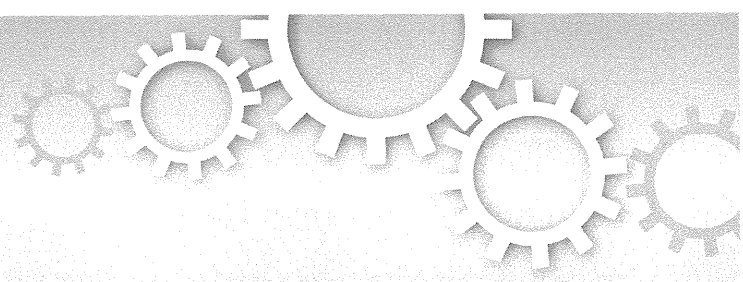

OPEN

SUBJECT AREAS:
TUMOUR SUPPRESSORS
CNS CANCER
BIOMARKER RESEARCH
DNA DAMAGE RESPONSE

Received
13 September 2012

Accepted
10 December 2012

Published
29 January 2013

Correspondence and requests for materials should be addressed to A.N. (akiranak@chiba-cc.jp)

* These authors contributed equally to this work.

Temozolomide suppresses *MYC* via activation of TAp63 to inhibit progression of human glioblastoma

Tomohiro Yamaki[1,2*], Yusuke Suenaga[1*], Toshihiko Iuchi[3], Jennifer Alagu[1], Atsushi Takatori[1], Makiko Itami[4], Akinobu Araki[4], Miki Ohira[5], Masahiro Inoue[6], Hajime Kageyama[7], Sana Yokoi[7], Naokatsu Saeki[2] & Akira Nakagawara[1]

[1]Division of Biochemistry and Innovative Cancer Therapeutics, Chiba Cancer Center Research Institute, 666-2 Nitona, Chuo-ku, Chiba 260-8717, Japan, [2]Department of Neurological Surgery, School of Medicine, Chiba University, 1-8-1 Inohana, Chuo-ku, Chiba 260-8670, Japan, [3]Division of Neurosurgery, Chiba Cancer Center, 666-2 Nitona, Chuo-ku, Chiba 260-8717, Japan, [4]Division of Surgical Pathology, Chiba Cancer Center, 666-2 Nitona, Chuo-ku, Chiba 260-8717, Japan, [5]Laboratory of Cancer Genomics, Chiba Cancer Center Research Institute, 666-2 Nitona, Chuo-ku, Chiba 260-8717, Japan, [6]Department of Biochemistry, Osaka Medical Center for Cancer and Cardiovascular Diseases, 1-3-3 Nakamichi, Higashinari-ku, Osaka 537-8511, Japan, [7]Cancer Genome Center, Chiba Cancer Center Research Institute, 666-2 Nitona, Chuo-ku, Chiba 260-8717, Japan.

Glioblastoma multiforme (GBM) is a highly invasive and chemoradioresistant brain malignancy. Temozolomide (TMZ), a DNA-alkylating agent, is effective against GBM and has become the standard first-line drug. However, the mechanism by which TMZ regulates the progression of GBM remains elusive. Here, we demonstrate that TMZ targets TAp63, a p53 family member, inducing its expression to suppress the progression of human GBM. High levels of *TAp63* expression in GBM tissues after TMZ treatment was an indicator of favourable prognosis. In human GBM cells, TMZ-induced TAp63 directly repressed *MYC* transcription. Activation of this TAp63-*MYC* pathway by TMZ inhibited human GBM progression both *in vitro* and *in vivo*. Furthermore, downregulation of *MYC* mRNA levels in recurrent GBMs after TMZ treatment correlated with better patient survival. Therefore, our results suggest that the TAp63-mediated transcriptional repression of *MYC* is a novel pathway regulating TMZ efficacy in GBM.

Glioblastoma multiforme (GBM) has been resistant to a variety of chemotherapeutic regimens for the last half-century and the average survival duration of patients was previously about 12 months[1,2]. In 2005, however, temozolomide (TMZ) was reported to be effective against GBM and to increase the survival period by an average of three months[3]. The survival advantage conferred by TMZ is largely restricted to GBMs with a methylated promoter status of the DNA-repair gene O^6-methylguanine-DNA methyltransferase (*MGMT*)[4]. MGMT repairs cytotoxic O^6-methylguanine adducts induced by TMZ, and thus the expression of *MGMT* contributes to TMZ-resistance in GBM[4,5]. Nevertheless, the molecular mechanism by which TMZ achieves its effect on GBM has remained elusive[2,6].

The p53 tumour suppressor family includes p63 and p73 members[7–9]. The TAp63 and TAp73 isoforms, which bear transactivation domain, function similarly to the p53 tumour suppressor by inducing apoptosis following DNA damage[10], while ΔNp63 and ΔNp73, which lack this domain, act as oncogenes[11]. The p53 signalling pathway is often altered in human GBM[12]; however, there have been no reports on the function of p63 and p73 in GBM. Therefore, we focused on the roles of p63 and p73 in GBM to investigate the mechanisms of DNA damage-induced activation of the other p53 family members following TMZ treatment. In this study, we show that TMZ activates TAp63 to repress *MYC* transcription, and that the downregulation of *MYC* by TAp63 augments the efficacy of TMZ in human GBM by suppressing proliferation and invasion.

Results

High TAp63 expression correlates with favorable prognosis in human GBM. To investigate the expression levels of p63 and p73 in human GBM, 69 newly diagnosed malignant gliomas (59 GBMs; 7 anaplastic astrocytomas; 3 anaplastic oligoastrocytomas) were selected for RNA and DNA analyses (Supplementary Table S1). Forty-nine cases had received procarbazine, ACNU and vincristine (PAV) therapy and twenty had

received TMZ therapy. First, our clinical data showed that TMZ treatment significantly prolonged the survival period of patients with malignant glioma (P = 0.0394; Supplementary Fig. S1a), and that high levels of *MGMT* expression were significantly associated with unfavourable prognoses (P = 0.0015; Supplementary Fig. S1b). Following quantitative RT-PCR for the analysis of *TAp63* and *TAp73* expression, the samples were divided into groups with high or low levels of *TAp63* (Fig. 1a) and *TAp73* (Supplementary Fig. S2) based on their respective expression levels in a normal adult brain. Kaplan–Meier cumulative survival curves showed that high *TAp63* expression was significantly associated with prolonged survival (P = 0.0373; Fig. 1b). In contrast, the levels of *TAp73* expression showed no prognostic potential (Supplementary Fig. S2). Therefore, from here on we focused on *TAp63* and selected the 20 TMZ-treated GBM samples to perform immunohistochemical staining for p63. We found that p63 immunopositivity (Fig. 1c) was significantly associated with better recurrence-free survival (P = 0.0066, Fig. 1d), and as *ΔNp63* mRNA was not detectable in these samples (data not shown), the positive p63 immunohistochemical staining may largely reflect the expression levels of TAp63 protein. Therefore, a high expression level of TAp63 is a favourable prognostic indicator of human GBM for cases that undergo TMZ treatment.

TAp63 directly represses *MYC* transcription in response to TMZ. Since other DNA damaging agents activate TAp63 by inducing its mRNA expression[13], we next investigated the role of TMZ in TAp63 expression. The steady-state mRNA levels of *TAp63* in four human GBM cell lines were analysed (Supplementary Fig. S3a), and *TAp63* isoforms was the major TAp63 isoform expressed (Supplementary Fig. S3b). TMZ stimulated TAp63 expression in both *TP53* mutant (YH-13) and wild-type (U87MG) cells, and induced the expression of TAp63 target genes, including *BAX*, *CDKN1A* (*p21*) and *MDM2* (Fig. 2a; Supplementary Fig. S4). In recent reports on functional network modelling analyses of GBM, a significant association between the p53 and MYC pathways has been suggested[14,15]. In addition, deletions of *TP53* and *PTEN* in murine brains caused the spontaneous development of GBM with a simultaneous induction of *MYC*[16]. Therefore, we examined the expression of *MYC* in TMZ-treated GBM. Interestingly, TMZ induced *TAp63* expression and suppresses *MYC* expression in a dose-dependent manner in both U87MG and YH-13 cells (Fig. 2a). Immunoblotting also showed an increase in TAp63 with suppression of MYC (Fig. 2b). Since p53 is reported to directly repress *MYC* transcription[17,18], we investigated whether TAp63 could regulate the transcription of *MYC*. Regardless of the status of *TP53*, siRNA knockdown of *TAp63* induced MYC expression at both the mRNA (Fig. 2c; Supplementary Fig. S5a) and protein (Fig. 2d) levels, whereas *TAp63* overexpression suppressed *MYC* (Fig. 2e; Supplementary Fig. S5b) and induced *BAX*, *CDKN1A* and *MDM2* (Supplementary Fig. S6a,b). *MYCN* levels remained unaffected in GBM cell lines (Supplementary Fig. S7a,b). To further confirm if TAp63-mediated suppression of *MYC* occurred in primary GBM cells, we introduced

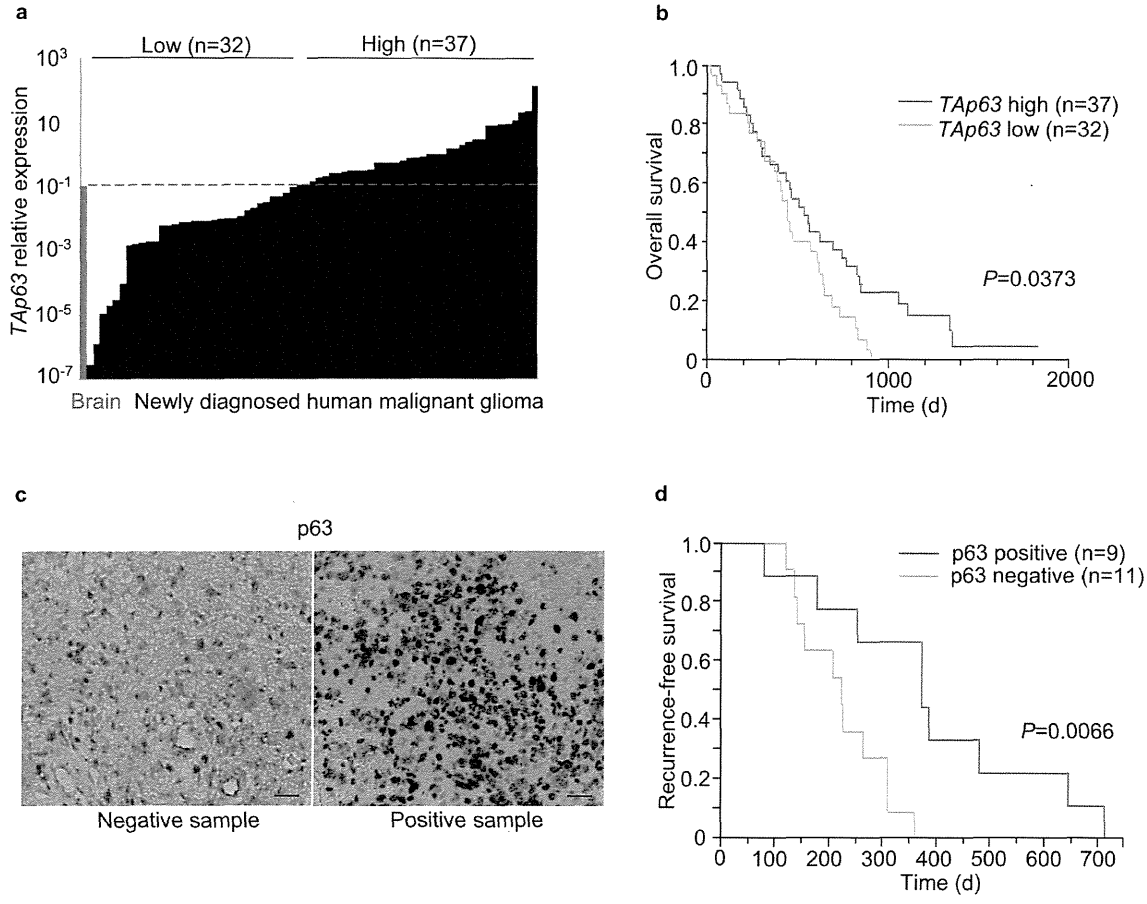

Figure 1 | High TAp63 expression correlates with favourable prognoses in human GBM. (a) *TAp63* mRNA expression detected by quantitative RT-PCR (qRT-PCR) in 69 newly diagnosed malignant glioma samples (59 GBM; 7 anaplastic astrocytoma; 3 anaplastic oligoastrocytoma). *TAp63* expression was normalised to *ACTB* mRNA, and designated high (n = 37) or low (n = 32) based on the normal human brain expression (dashed red line). (b) Overall survival of subjects with newly diagnosed malignant gliomas according to relative *TAp63* expression levels before chemotherapy (n = 69; high, n = 37; low, n = 32). P value by log-rank test. (c) p63 immunohistochemical staining in human GBM. Scale bar, 50 μm. (d) Recurrence-free survival of 20 TMZ-treated GBM subjects according to p63 immunohistochemical staining in newly diagnosed samples. P values by log-rank test.

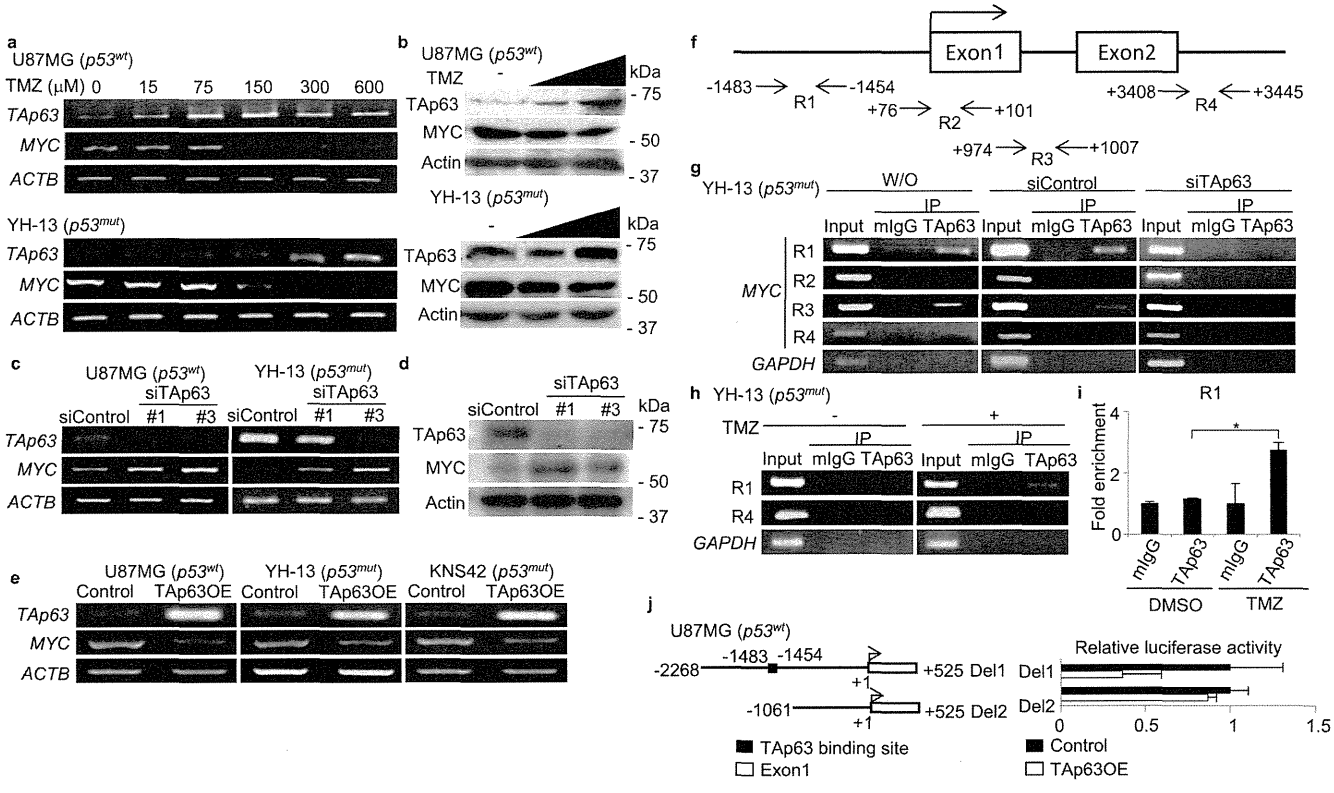

Figure 2 | TMZ-induced TAp63 suppresses *MYC* expression in human GBM cells. (a) *TAp63* and *MYC* mRNA levels in GBM cells with increasing TMZ concentrations, 24 h. (b) Immunoblot of TAp63 and MYC from GBM cells treated with increasing concentrations of TMZ, 24 h. (c) RT-PCR analyses of relative *MYC* expression in U87MG and YH-13 cells following siTAp63 transfection, normalised to *ACTB* mRNA. (d) Analysis of MYC expression in YH-13 cells transfected with siControl or siTAp63 by western blotting. (e) RT-PCR analyses showing *MYC* suppression after *TAp63α* overexpression in GBM cell lines. (f) Positions of PCR primer sets R1, R2, R3 and R4 for the chromatin immunoprecipitation (ChIP) assays. (g) Identification of the TAp63-binding region in the *MYC* promoter by ChIP assays. YH-13 cells were transfected with or without indicated siRNAs. Genomic DNA was amplified by PCR using the indicated primers. (h) Semi-quantitative PCR and (i) quantitative PCR of ChIP assays showing endogenous TAp63 recruitment onto the *MYC* promoter after 24 h TMZ treatment, 150 μM. $^*P < 0.005$ (two-tailed *t*-test). (j) Luciferase activity of *MYC* reporters after lentiviral *TAp63α* or GFP infection of U87MS cells. Data shown as the fold change in the luciferase activity compared with control cells.

the use of cancer tissue-originated spheroids (CTOS) composed of pure tumor cells derived directly from the GBM tissue[19]. As shown in Supplementary Fig. S8, the TAp63-*MYC* regulatory pathway was intact in the CTOS. To examine whether TAp63 directly represses *MYC* transcription, we performed a chromatin immunoprecipitation (ChIP) assay. We designed four primer sets (R1, R2, R3 and R4) to amplify the indicated genomic regions of the putative TP53 binding sequence (Fig. 2f). Our results showed that endogenous TAp63 was recruited to the upstream promoter and the intron 1 region of the *MYC* gene in YH-13 cells, but not intron 2, which has been previously shown as a p53-binding site[18] (Fig. 2g). In response to TMZ treatment, the amount of TAp63 recruited onto the *MYC* promoter was significantly increased (Fig. 2h,i), however, there was no increase in TAp63 recruitment onto intron 1 (Supplementary Fig. S9). *TAp63* overexpression in YH-13 and U87MG cells inhibited *MYC* promoter activity (Fig. 2j; Supplementary Fig. S10), suggesting that TMZ stimulates the TAp63-mediated repression of *MYC* transcription in GBM cells.

The TAp63-*MYC* pathway regulates sphere formation and invasion in GBM. *MYC* is a regulator of stemness in glioma, and its expression is required for glioma cell neurosphere formation[20]. Consistent with these notions, *TAp63* knockdown increased both the number and size of YH-13 neurospheres, while knockdown of *MYC* suppressed the sphere-forming ability (Fig. 3a,b). Moreover, the number of spheres formed by YH-13 cells co-transfected with both siTAp63 and siMYC was less than that of cells transfected with siTAp63 alone, suggesting that *MYC* induction by TAp63 knockdown contributes to the sphere-forming ability of tumour cells.

TAp63 also plays a critical role in the regulation of cancer invasion[21,22]. To assess whether the TAp63-*MYC* pathway also regulates invasion, *TAp63* and *MYC* were knocked down in YH-13 cells with siRNA for 24 and 48 h. Although knockdown of endogenous *TAp63* and *MYC* had no effect on cell proliferation by day 2 of culture (Fig. 3c), knockdown of *TAp63* alone significantly promoted the cellular invasion of YH-13 cells. Additionally, co-transfection of siTAp63 and siMYC decreased the percentage of invading cells compared to siControl-transfected cells (Fig. 3d), suggesting that TAp63 downregulates GBM invasion via *MYC* suppression.

Temozolomide suppresses tumour cell growth and invasion via TAp63 induction. We assessed whether TMZ affects the invasive property of GBM cells via the TAp63-*MYC* pathway. The treatment of U87MG cells with 75 μM TMZ inhibited cell proliferation and significantly inhibited cellular invasion on day 5 of exposure (Fig. 4a,b). Since apoptotic cell death was not observed under these experimental conditions (Supplementary Fig. S11), TMZ may have anti-invasive properties. Moreover, U87MG cells were transfected with the indicated siRNAs for *TAp63* and *MYC* and subjected to Boyden chamber invasion assays. *TAp63* knockdown in U87MG cells induced *MYC* mRNA expression and rescued the TMZ-inhibited cellular invasion, compared to the control (Fig. 4c). Next, to assess the antitumour effects of TAp63 *in vivo*, we knocked down

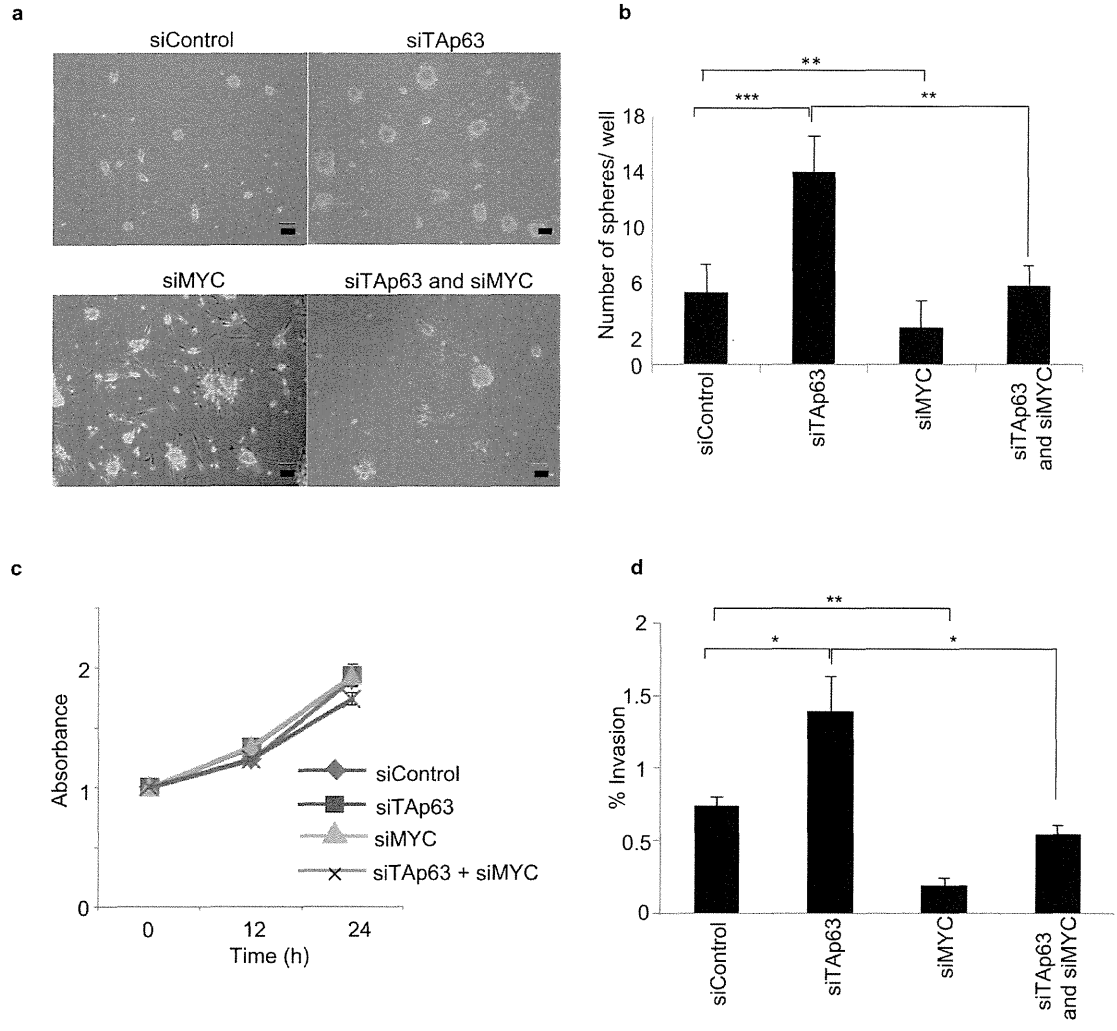

Figure 3 | TAp63-*MYC* pathway is critical for glioblastoma sphere-forming ability and invasion *in vitro*. (a) Sphere formation assay of YH-13 cells, showing induction of sphere-forming activity after knockdown of *TAp63* and *MYC*. (b) The graph indicates the differences in the sphere numbers per microscopic field at 400× magnification. The values represent the mean ± SD of triplicate samples from a single representative experiment (n = 9). $^{**}P < 0.0005$, $^{***}P < 0.00005$ (two-tailed *t*-test). (c) Cell viability assay of *TAp63* and *MYC* knockdown in YH-13 cells. (e) The graph indicates the percentage of YH-13 cells invading the Matrigel relative to control migration, following *TAp63* and *MYC* knockdown. $^{*}P < 0.05$, $^{**}P < 0.0005$ (two-tailed *t*-test).

TAp63 in the tumors of U87MG xenograft mouse models. Our results showed that TAp63 knockdown promotes tumour cell proliferation (Supplementary Fig. S12a,b). To investigate the role of TAp63 in TMZ efficacy, we implanted U87MG cells into the hind legs of mice (n = 4) and, 7 days later, injected siControl and siTAp63 into the palpable tumours, which were then treated with TMZ (15 mg/kg) intraperitoneally on the same day. At day 14, tumours subjected to siTAp63 knockdown with TMZ treatment were considerably larger compared to the control tumours, indicating a drug-resistant phenotype (Fig. 4d). Finally, we assessed whether the TMZ-induced activation of the TAp63-*MYC* pathway is associated with the clinical outcome of patients. To this end, we analysed the RNA from 20 paired (initially diagnosed tumour and recurrent tumour from the same patient) malignant glioma samples (17 GBMs, three anaplastic oligoastrocytomas) from TMZ-treated patients. The expression levels of *MYC* mRNA were significantly decreased after the treatment (Fig. 4e). Furthermore, the subgroup with decreased *MYC* expression after TMZ treatment showed significantly better overall survival (Fig. 4f). We performed a similar analysis using only the GBM mRNA data and both *TAp63* expression and *MYC* suppression indicated good prognoses (Fig S13a–f). Taken together, these findings suggest that the TMZ-mediated suppression of *MYC* via TAp63 activation is a key pathway for the drug's efficacy against GBM.

Discussion

In this study, we report that TAp63 regulates *MYC* transcription and tumor progression in TMZ-treated GBM. The study highlighted four points. First, TAp63 expression is a favourable prognostic factor in TMZ-treated GBM. Second, TMZ induces TAp63 to suppress growth and invasion. Third, TAp63 directly represses *MYC* expression in response to TMZ treatment, and fourth, *MYC* downregulation correlates with TMZ efficacy.

A possible mechanism of TMZ action could be that TMZ induces *TAp63* expression in GBM cells, and in turn, activated TAp63 inhibits cellular invasion via suppression of *MYC* expression. These findings are consistent with the previous reports in which TAp63 suppresses invasion through coordinated transcriptional regulation of its downstream target genes such as *SERPINB5, CCNG2, BHLHE41* and *DICER1*[21–24].

A prior study on the regulatory mechanisms of p53 upon its downstream targets showed that in response to hypoxic stress, p53 is recruited onto intron 2 of the *MYC* gene to directly inhibit *MYC* transcription[18]. Our work has identified a critical role for TAp63 as

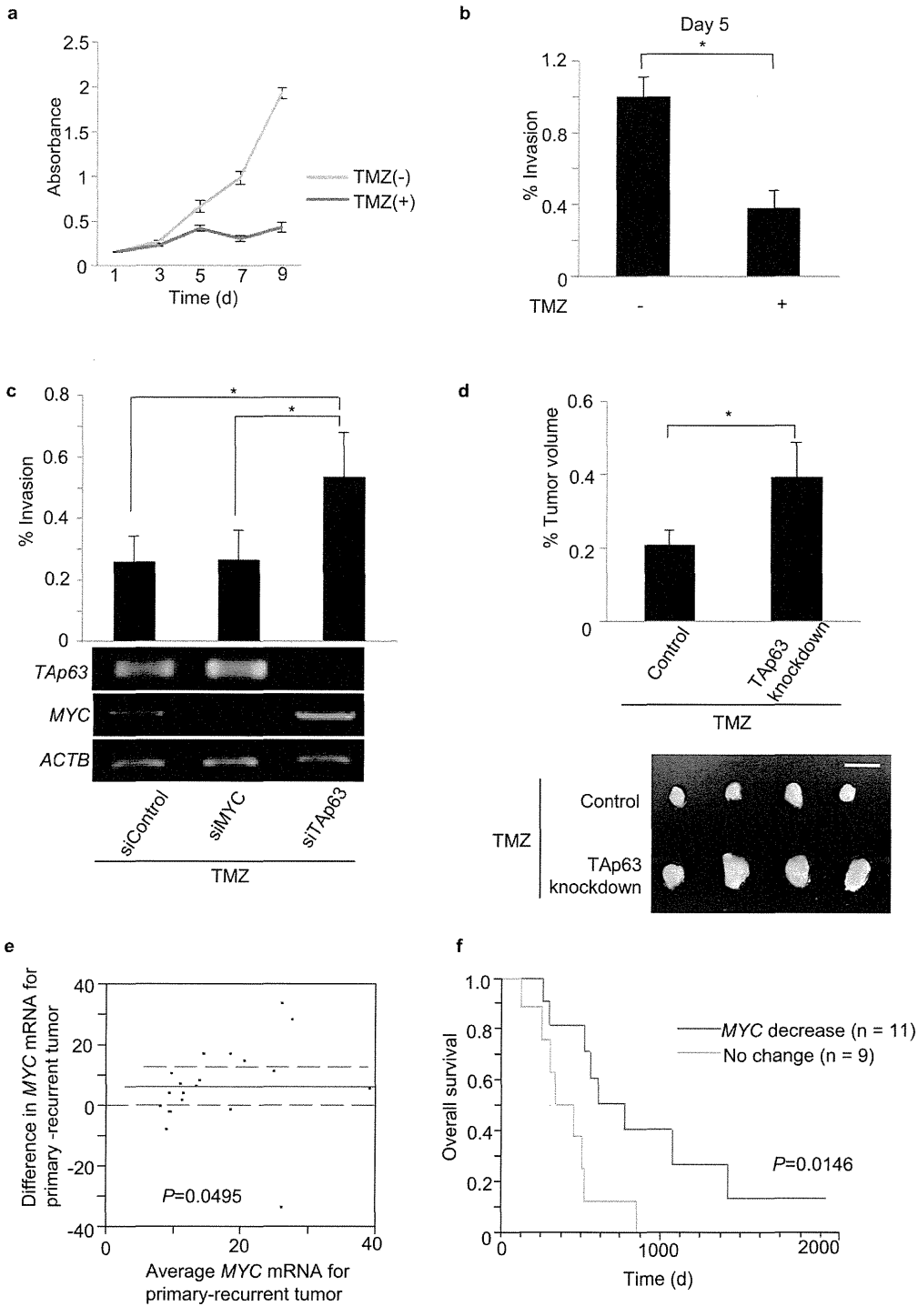

Figure 4 | TMZ inhibits GBM progression via the TAp63-*MYC* pathway. (a) Cell viability assay showing suppression of proliferation in cells treated with TMZ, 75 μM. (b) Cellular invasion was suppressed by day 5, at which point the treated and control cultures were adjusted to 5×10^4 cells/500 μl and subjected to Boyden chamber invasion assays. $^*P < 0.05$ (two-tailed *t*-test). (c) Percentage of U87MG cells invading the Matrigel relative to control migration, following *TAp63* knockdown and TMZ treatment. Corresponding mRNA analysis. $^*P < 0.05$ (two-tailed *t*-test). (d) Effect of *TAp63* knockdown on the U87MG cells treated with TMZ treatment at 14 days after subcutaneous transplantation in nude mice. The end volumes were compared to the volumes at implantation. Tumour growth was measured with callipers and calculated by the formula: volume = length (A) × width (B) × width (B) × 0.5, where A and B are the long and short axes respectively. TMZ in PBS was administered intraperitoneally at 15 mg/kg once a week. Data are representative of five independent experiments (n = 4). $^*P < 0.05$ by two-tailed *t*-test. Photographs in (d) are representative of n = 4 mice. Bar, 10 mm. (e) *MYC* downregulation in recurrent tumours after TMZ plus radiotherapy (n = 20; solid line: mean difference; dashed lines: 95% confidence interval. *P* value by paired *t*-test. (f) Overall survival according to *MYC* downregulation (≥1.5-fold decrease in primary/recurrent (p/r) *MYC* mRNA), post-TMZ treatment. *MYC* decrease: n = 11, mean p/r = 2.65 ± 0.31 s.d.; no change: n = 9, mean p/r = 0.9 ± 0.13 s.d. *P* value by log-rank test.